Characteristics of atmospheric boundary layer height over the Arctic Ocean during MOSAiC

Shijie Peng [1], Qinghua Yang [1], Matthew D. Shupe [2,3],

Xingya Xi [1], Bo Han [1], Dake Chen [1], Sandro Dahlke [4], Changwei Liu [1*]

1 School of Atmospheric Sciences, Sun Yat-sen University, and Southern Marine Science and Engineering Guangdong Laboratory (Zhuhai), Zhuhai 519082, China

2 Cooperative Institute for Research in Environmental Sciences, University of Colorado Boulder, Boulder, CO, USA

3 NOAA Physical Science Laboratory, Boulder, CO, USA

4 Helmholtz Centre for Polar and Marine Research, Alfred Wegener Institute (AWI), Potsdam, Germany

Correspondence to: Changwei Liu (liuchw8@mail.sysu.edu.cn)

Abstract

The important roles of the atmospheric boundary layer (ABL) in the central Arctic climate system have been recognized, but the atmospheric boundary-layer height (ABLH), defined as the layer of continuous turbulence adjacent to the surface, has rarely been investigated. Using a year-round radiosonde dataset during the Multidisciplinary drifting Observatory for the Study of Arctic Climate (MOSAiC), we improve a Richardson-number-based algorithm that takes cloud effects into consideration, and analyze the characteristics and variability of ABLH over the Arctic Ocean. The results reveal that the annual cycle is clearly characterized by a distinct peak in May and two minima in January and July. This annual variation in ABLH is primarily controlled by the evolution of ABL thermal structure. Temperature inversions in the winter and summer are intensified by seasonal radiative cooling and surface melting, respectively, leading to the low ABLH at these times. Near-surface conditions (e.g., friction velocity) also play a significant role in ABLH variation, and the ABLH can be roughly estimated based on these basic variables. In addition, the MOSAiC ABLH is more suppressed than the ABLH during the Surface Heat Budget of the Arctic Ocean (SHEBA) experiment in the summer, which indicates that there is large variability in the Arctic ABL structure during summer melting season.

1 Introduction

In recent years, the rapidly changing climate and declining sea ice in the Arctic have been reported by numerous studies (e.g., Matveeva and Semenov, 2022; Meier and Stroeve, 2022; Esau et al., 2023). The Arctic near-surface temperature is increasing at a rate 2–3 times larger than the global average, which is referred to as Arctic amplification (Overland et al., 2019; Blunden and Arndt, 2019), and the Arctic has entered the 'new Arctic' period (Landrum and Holland, 2020). As a key component of the Arctic climate system, the atmospheric boundary layer (ABL) over the Arctic Ocean is closely associated with Arctic warming and has a big impact on sea ice loss (Francis and Hunter, 2006; Graversen et al., 2008; Wetzel and Bruemmer, 2011). Thus, it is critical to improve our understanding of Arctic ABL processes under 'new Arctic' conditions.

The ABL structure over the Arctic Ocean has unique characteristics due to the presence of semipermanent

sea ice, and is shaped by various mechanisms including interactions with the surface, free atmosphere, and wave activity. Most studies of the Arctic ABL structure have been based on coastal observatories and limited drifting ice stations (Knudsen et al., 2018; Vullers et al., 2021). It has been found that a predominant temperature inversion in the lower troposphere exists in all seasons and is referred to as the "Arctic inversion" (Andreas et al., 2000; Tjernström et al., 2009). The Arctic inversion is sometimes elevated, with regions of near-neutral stability below the inversion (Persson et al., 2002; Tjernström et al., 2012). The Arctic vertical structure is influenced by many factors, such as warm-air advection, surface melt, cloud-top cooling, and turbulent mixing (Busch et al., 1982; Vihma et al., 2011; Vihma, 2014). Investigations of the ABL structure evolution and its controlling factors are the keys to knowing the ABL's role in the Arctic atmosphere (Sterk et al., 2014).

The atmospheric boundary-layer height (ABLH), here defined as the height of continuous turbulent mixing extending up from the surface, is the key indicator of the ABL structure (Seibert et al., 2000; Seidel et al., 2012). It determines the vertical extent of many atmospheric processes, such as convective transport and aerosol distributions, and is an important parameter for weather and climate models (Holtslag et al., 2013; Mahrt, 2014; Davy and Esau, 2016). In some previous studies, the ABLH over the Arctic Ocean is defined as the height of the surfaced-based inversion top or the capping inversion base (e.g., Tjernström et al., 2009; Sotiropoulou et al., 2014). However, as the most fundamental characteristic of the ABL, turbulence is not fully considered in this definition. There are two primary layers of turbulent mixing in the Arctic atmosphere. First, the surface layer, formed by turbulent mixing processes near the surface, is frequently shallower than the Arctic inversion layer (Mahrt, 1981; Andreas et al., 2000). Second, the turbulence associated with low-level clouds, which is driven by radiative cooling near the cloud top, forms a cloud-induced mixed layer (Solomon et al., 2011; Shupe et al., 2013). This cloud-driven mixed layer is sometimes decoupled from the surface mixed layer while at other times it extends down to form a coupled, well-mixed layer all the way to the surface (Shupe et al., 2013; Brooks et al., 2017). Wind-shear induced turbulence can also play a role in both of these layers and their interactions. Based on different turbulence characteristics, the ABLH is commonly determined using profiles of potential temperature, wind speed, and humidity, and various methods have been proposed for calculating ABLH (Seibert et al., 2000; Seidel et al., 2010). However, the applicability of these methods in the Arctic needs to be further assessed.

Due to the lack of observations, there are few analyses of ABLH over the Arctic Ocean based on observational data. Distributions of Arctic ABLH have been investigated by Tjernström and Graversen (2009), Liang and Liu (2010), and Dai et al. (2011), but their studies are all based on the Surface Heat Budget of the Arctic Ocean (SHEBA) campaign conducted 25 years ago (Uttal et al., 2002). To improve our understanding of the ABL structure and ABLH characteristics under "new Arctic" conditions, we need new, comprehensive observations in this environment. The Multidisciplinary drifting Observatory for the Study of Arctic Climate (MOSAiC) expedition was, in part, designed to achieve this goal (Shupe et al., 2022). Based on and around a drifting research vessel in the central Arctic for a whole year, the MOSAiC expedition provided a wealth of data and related data products with unprecedented high temporal resolution and year-round temporal coverage. These data make possible a more detailed analysis of the ABL structure evolution

77 and ABLH variability.

78 In this study, based on observational data from the MOSAiC expedition, we propose an improved ABLH

79 algorithm and then examine the characteristics of the ABL evolution over the 'new Arctic' sea-ice surface.

80 This paper is organized as follows: Section 2 briefly describes the MOSAiC expedition and the observations;

81 section 3 provides an ABLH determination method to evaluate several automated algorithms, and develops

82 an improved ABLH algorithm; section 4 presents the results of ABLH variation over the annual cycle, the

83 controlling factors of ABLH variation, and mechanisms of ABL development and suppression; section 5

84 compares the difference in ABLHs between SHEBA and MOSAiC; and conclusions are given in section 6.

85

2 Measurements

87 In this study, the SHEBA-based sounding data (Moritz, 2017) and multiple MOSAiC data are used. Here

88 we mainly introduce the MOSAiC expedition. The MOSAiC track is shown in Fig. 1, which is based on the

89 research vessel *Polarstern* (Knust, 2017), with the main period of atmospheric state observations starting in

90 October 2019 and ending in September 2020. *Polarstern* drifted across the central Arctic Ocean and

91 navigated through the sea ice north of 78° N during most of the MOSAiC year. The whole drifting period is

92 divided into five parts, and the vessel sailed in the gap period between some of those parts. More details are

93 provided in Shupe et al. (2022). The following are the descriptions of the instruments and data products used

94 in this paper.

95

2.1 Radiosonde observations and relevant data products

97 The radiosonde data were obtained through a partnership between the leading Alfred Wegener Institute

98 (AWI) , the atmospheric radiation measurement (ARM) user facility, a US Department of Energy facility

99 managed by the Biological and Environmental Research Program, and the German Weather Service (DWD)

100 (Maturilli et al., 2022). Vaisala RS41-SGP Radiosondes were regularly launched on board throughout the

101 whole MOSAiC year (from October 2019 to September 2020), including periods when the vessel was in

102 transit. The sounding frequency is normally four times per day (launched at about 5:00, 11:00, 17:00, and

103 23:00 UTC) and is increased to 7 times per day during periods of exceptional weather or coordination with

104 other observing activities. The radiosoundings provide data on the atmospheric state, including vertical

105 profiles of pressure, temperature, relative humidity (*RH*), and winds, from 12 m up to 30 km with a vertical

106 resolution of 5 m. However, the sounding data below ~100 m altitude may be contaminated by the vessel

107 itself. To avoid contamination affecting our analysis, we use a merged data product that combines the

108 soundings with measurements from a meteorological tower on the sea ice away from the vessel, and was

109 specifically designed to minimize ship effects and provide more reliable profiles in the lowest 100 m, which

110 has been recently submitted (Dahlke et al., 2023). In this paper, data quality control and a six-point moving

111 average in height are applied to the merged profile data to eliminate invalid data and measurement noise,

112 and all data are interpolated onto a regular vertical grid with 10 m intervals. In total, there are 1484 sounding

113 profiles available. In addition, DOE-ARM provides a Planetary Boundary Layer Height Value-Added

114 Product (PBLHT VAP, Riihimaki et al., 2019), which uses several different automated algorithms to compute

115 ABLH estimates based on radiosonde profiles. This VAP provides 964 ABLH estimates, and we select 914
116 samples from these to ensure that the estimates obtained by all algorithms are available.
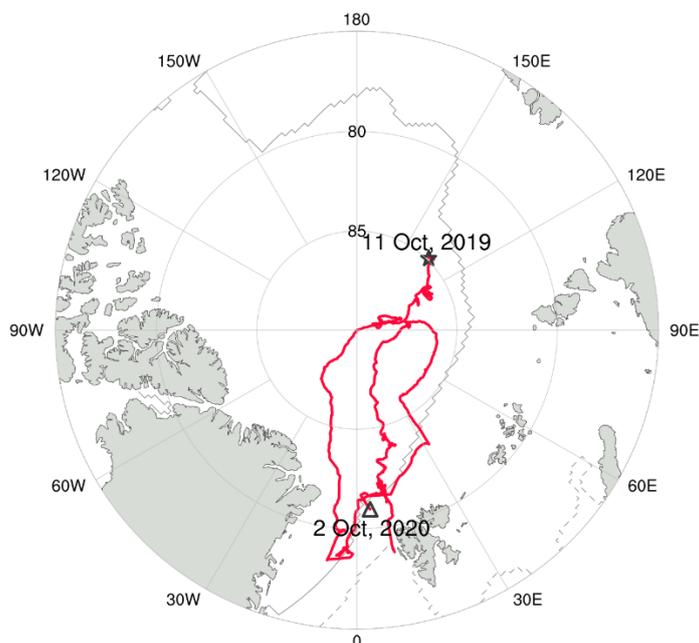
118 Figure 1 The MOSAiC expedition track from (star) 11 October 2019 through to (triangle) 2 October 2020 is
119 plotted by the red line. Gray solid and dashed lines denote the approximate sea ice edge at the minimum (15
120 September 2020) and the maximum (5 March 2020), respectively.

2.2 Meteorological and turbulence measurements near the surface

123 Meteorological and turbulence measurements were made from a tower on the sea ice at "Met City",
124 which was located 300–600 m away from the vessel (Cox et al., 2023). The u-Sonic-3 Cage MP anemometers
125 by METEK GmbH and HMT300 air temperature sensors by Vaisala were fixed at nominal heights of 2 m, 6
126 m, and 10 m on the meteorological tower. The tower was set up during the periods when the vessel passively
127 drifted with an ice floe (i.e., from mid-October 2019 to mid-May 2020, from mid-June through July 2020,
128 and from late August to mid-September 2020). The sampling frequency of fast response instruments (i.e., u-
129 Sonic-3 Cage MP anemometer) was at 20 Hz, resampled to 10 Hz. To derive turbulence parameters, the
130 following processes were carried out: despiking, block averaging over a 10-min interval, coordinate rotating
131 via double rotation, frequency correcting, and virtual temperature correcting. In this study, sensible heat flux
132 (*SH*, defined as positive upwards), near-surface air temperature at 2 m, friction velocity, and turbulent kinetic
133 energy (TKE) dissipation rate are used. Based on a footprint analysis using the Kljun et al. (2015) model,
134 90% of the sensible heat flux measurements have a source area fetch of no more than 275 m, a region that
135 was typically strongly dominated by consistent sea ice throughout the year. Although the sounding site may
136 typically be outside the source region of these flux measurements, we assume the conditions at the two sites
137 are predominantly equivalent, which is also assumed in the merged sounding-tower product.

2.3 Cloud properties derived from combined sensors

140   Cloud-related measurements come from ShupeTurner cloud microphysics product (Shupe, 2022). This
141   product uses multiple measurement sources (e.g., cloud radar, ceilometer, depolarization lidar, and
142   microwave radiometer) to derive time-height data, including cloud phase type and condensed water content
143   for both liquid and ice. Details of the retrieval algorithm, its application, and uncertainties are provided in
144   Shupe et al. (2015). In our study, the condensed water content data are linearly interpolated onto the vertical
145   grid with resolution of 10 m for consistency. The cloud phase type data are used to determine clear and
146   cloudy environments. A grid point is labeled as "cloudy" if clouds are identified in the upper and lower cloud
147   phase type data points adjacent to the grid, otherwise it is labeled as "clear".

148

149   **3 ABLH determination method and algorithm evaluation**

150   The most objective method of ABLH determination is based on profiles of turbulence measurements
151   deployed on aircraft or other platforms, but such measurements were not routinely carried out during the
152   MOSAiC expedition. Thus, the ABLH determination in our study is based on the thermal and dynamic
153   structure of radiosoundings. In previous literature, the ABLH is determined through multiple profiles of
154   atmospheric variables and manual visual inspection, which can be considered as the "observed" ABLH
155   (Liang and Liu, 2010; Zhang et al., 2014; Jozef et al., 2022). In this section, we will describe the manually-
156   labeled ABLH determination method and derive an ABLH for each sounding. Next, we will use these ABLHs
157   as a reference to evaluate the automated ABLH algorithms provided by the PBLHT VAP. Finally, we will
158   develop and evaluate an improved ABLH automated algorithm that is suitable for the Arctic atmosphere,
159   and further discuss an important parameter for the algorithms and its stability dependence.

160

161   **3.1 ABL regime classification and ABLH determination**

162   The ABLH determination method starts with the classification of ABL regimes. Based on previous
163   studies (e.g., Vogelezang and Holtslag, 1996; Liang and Liu, 2010), we divide the ABLs into three types:
164   stable boundary layer (SBL), near-neutral boundary layer (NBL), and convective boundary layer (CBL),
165   corresponding with three different stability states near the surface. We first use SH to diagnose the ABL
166   regime types. The specific classification formula is presented below:

167
$$\begin{cases} SH > +\delta & \text{for CBL} \\ SH < -\delta & \text{for SBL}, \ (1) \\ \text{else} & \text{for NBL} \end{cases}$$

168   where δ is the critical value that is specified as 2 W m^{-2}, following Steeneveld et al. (2007b). If corresponding
169   SH data are unavailable, the difference of equivalent potential temperature (θ_E) between the 100 and 50 m
170   heights (θ_E difference) derived from the sounding profile is used to determine the ABL type. Specifically, if
171   θ_E difference is larger than 0.2 K, the ABL is identified as SBL; if θ_E difference is less than -0.2 K, the ABL
172   is identified as CBL; and other profiles are labeled as NBLs, roughly following Liu and Liang (2010).

173   The manually-labeled ABLH determination in our study is based on characteristics of sounding profiles
174   and regime types. For each atmospheric sounding profile, equivalent potential temperature (θ_E), equivalent
175   potential temperature gradient (θ_{Egrad}), wind speed (WS), specific humidity (q_v), and RH are used to obtain
176   multiple estimates of the ABLH, which are used to determine the final estimate. Three cases to describe the

method are presented in Fig. 2. Figures 2 (a–c) are the case of a SBL, which features surface-based temperature and humidity inversions. Figures 2 (d–f) are the case of a NBL, with approximately constant θ_E from the surface up to the inversion base and strong horizontal wind. Figures 2 (g–i) are the case of a CBL, with a deeper well-mixed layer and low-level cloud coupled to the surface (e.g., Shupe et al., 2013). In terms of θ_E profiles, the estimated ABLH is the level at which the θ_{Egrad} reaches its maximum for SBL and NBL cases, and the base of the θ_E inversion for CBL cases (Martucci et al., 2007). In terms of *WS* profiles, the ABLH is estimated to be the height of the WS maximum for all three regime types (Mahrt et al., 1979). In terms of humidity profiles, the estimated ABLH is the level at which the *RH* rapidly decreases for SBL and NBL cases, and the base of the q_v inversion for CBL cases (Lenschow et al., 2000). The manually-observed ABLHs (solid black lines in Fig. 2) are then determined through consideration of these three distinct estimates using the following rules: (1) If the estimates differ slightly from each other, take the average of these estimates as ABLH; (2) If a strong characteristic (sharp gradients or peaks) of the profile is evident, select the estimate obtained based on this characteristic; (3) If the ABL structure is similar to that at the previous time, select the estimate with the smallest change to ensure that ABLHs are consistent in time. It is evident that the lowest layers of profiles have a great impact on the ABLH determination, particularly for shallow SBLs and NBLs. Thus, the merged radiosonde-tower profiles help make the ABLH determination more reliable than when using radiosondes alone.

Figure 2 Vertical profiles of (left) equivalent potential temperature (θ_E), θ_E gradients (θ_{Egrad}), (middle) wind speed (*WS*), and (right) relative humidity (*RH*) and specific humidity (q_v) at (a–c) 25 November 2019, 22:51 UTC, (d–f) 2 December 2019, 16:58 UTC, and (g–i) 17 December 2019 16:58 UTC. Boundary layers at the three times represent stable boundary layer (SBL), near-neutral boundary layer (NBL), and convective boundary layer (CBL), respectively. The gray dashed horizontal lines denote the atmospheric boundary-layer height (ABLH) estimates based on multiple profiles, and the black solid horizontal lines denote the manually observed ABLHs. The dots in the lowest 100 m denote the section of the profiles impacted by the radiosonde-tower merging.

3.2 Automated algorithm evaluation

The automated ABLH algorithms consist of various empirical formulas. Based on these empirical formulas, estimated ABLHs are determined automatically and without manual intervention. Therefore, these algorithms can perform real-time and fast calculations on large amounts of data and are widely used in model simulations (Seibert et al., 2000; Konor et al., 2009). However, automated algorithms might lead to large

210 errors in estimating ABLHs, and the parameter selection in these algorithms will have a great impact on the

211 results. In our study, estimated ABLHs obtained using three automated algorithms are compared with

212 manually-labeled ABLHs to evaluate their performance over the Arctic Ocean. These algorithms, including

213 the Liu-Liang algorithm, the Heffter algorithm, and the bulk Richardson number algorithm, are all available

214 in the PBLH VAP as described in Sivaraman et al. (2013). Here we give a brief description of the three

215 algorithms.

216 The Liu-Liang algorithm determines ABLH based on potential temperature and wind speed according to

217 Liang and Liu (2010). For CBL regimes, the definition of ABLH is the height at "which an air parcel rising

218 adiabatically from the surface becomes neutrally buoyant", and the temperature excess value is 0.1 K. For

219 SBL regimes, two different estimates of the ABLH are obtained, if possible, based on stability criteria and

220 wind shear criteria, respectively. For stability, the ABLH is defined as the lowest level, k, at which the θ_{Egrad}

221 reaches a minimum and meets either of the following two conditions:

222
$$\begin{cases} \theta_{Egrad\,k} - \theta_{Egrad\,k-1} < -40 \text{ K/km} \\ \theta_{Egrad\,k+1} < 0.5 \text{ K/km}, \theta_{Egrad\,k+2} < 0.5 \text{ K/km} \end{cases}, (2)$$

223 where the subscripts (k, k-1, k+1, and k+2) represent the θ_{Egrad} at corresponding levels. For wind shear, the

224 ABLH is defined as the height where the wind speed reaches a maximum that is at least 2 m/s stronger than

225 the layers immediately above and below while decreasing monotonically toward the surface (i.e., a low-level

226 jet). The final ABLH is defined as the lower of the two heights.

227 The Heffter algorithm, which was suggested by Heffter (1980), is a widely used algorithm (e.g., Marsik

228 et al., 1995; Snyder and Strawbridge, 2004). The algorithm determines ABLH through the strength of the

229 inversion and potential temperature difference across the inversion. The ABLH is defined as the lowest layer

230 in which the potential temperature difference between the top and bottom of the inversion is greater than 2

231 K. If no layer meets the criteria, the ABLH is defined as the layer at which the potential temperature gradient

232 reaches the largest maximum.

233 The bulk Richardson number algorithm is based on the profile of the bulk Richardson number (Ri_b), and

234 has been shown to be a reliable algorithm for determining ABLHs (Seidel et al., 2012). Ri_b is a dimensionless

235 number that represents the ratio of thermally produced turbulence to that induced by mechanical shear. The

236 Ri_b formula used in the PBLH VAP (Sørensen et al., 1998; Sivaraman et al., 2013) is expressed as:

237
$$Ri_b = \left(\frac{gh}{\theta_{v0}}\right)\left(\frac{\theta_{vh} - \theta_{v0}}{u_h^2 + v_h^2}\right), (3)$$

238 where g is the acceleration of gravity; θ_{vh} and θ_{v0} are the virtual potential temperature at height h and the

239 surface, respectively; u_h and v_h are the horizontal wind speed component at height h. The ABLH is defined

240 as the height of Ri_b exceeding a critical threshold (the critical bulk Richardson number, Ri_{bc}; Seibert et al.,

241 2000). The PBLH VAP includes ABLH estimates based on two widely used Ri_{bc} values: 0.25 and 0.5.

242 To quantitatively evaluate the performance of each automatic algorithm, we introduce the correlation

243 coefficient R and two other statistical measures: the $Bias$ and the median absolute error ($MEAE$; Steeneveld

244 et al., 2007a). The formulas are as follows:

245
$$Bias = \frac{2}{n}\sum_{i=1}^{n}\frac{H_{auto} - H_{obs}}{H_{auto} + H_{obs}}, (4)$$

$$MEAE = \mathrm{median}(|H_{auto}-H_{obs}|), (5)$$

where H_{auto} is the ABLH obtained by the automated algorithm; H_{obs} is the ABLH manually determined; n is the number of valid sounding profile samples. According to the definitions of these statistical measures, larger R and smaller *Bias* and MEAE mean a better performance of the automated algorithm.

We also analyze the algorithm performances for cloudy and clear conditions, considering that low-level clouds containing liquid water play an important role in the Arctic ABL (Shupe and Intrieri, 2004; Brooks et al., 2017). In our study, the *RH* threshold of 96% (Silber and Shupe, 2022) and the cloud source flag data are used for cloud detection. If a cloud is detected in the cloud source flag data and the *RH* is larger than 96%, then the profile is labeled as cloudy. The sounding profiles that contain at least one identified cloud layer below 1500 m are classified as "cloudy", and as "clear" otherwise.

Figure 3 presents the comparisons of estimated ABLHs with the manually-labeled ABLHs, and the associated statistical measures are given in Table 1. The results show that the Ri_b algorithm with Ri_{bc} of 0.25 performs best overall, and particularly for SBL cases. The performance of the Ri_b algorithm with Ri_{bc} of 0.5 is poorer than that of the Ri_b algorithm with Ri_{bc} of 0.25, with overestimations of ABLHs in general, and larger errors with lower correlation coefficients for all types of ABLs. The Heffter algorithm performs well in cases of high ABLH and particularly for cloudy and CBL cases, but does significantly overestimate ABLH in a large number of cases as shown in the Fig. 3c subgraph. This is attributed to the determination criterion of the Heffter algorithm, i.e., ABLHs are determined by inversion layers, which means that large errors occur when the inversion layer is higher than the mixed layer. Additionally, while the Heffter performance in many of the ABL conditions is only marginally worse statistically than the Ri_b algorithm with Ri_{bc} of 0.25, its correlations are notably worse for SBL and NBL cases. The performance of the Liu-Liang algorithm is generally poorer than the other algorithms, particularly for correlation coefficient, which is probably due to the impact of noise in the lower ABLH profiles and unsuitable parameters in the algorithm. In summary, the Ri_b algorithm is reliable over the Arctic Ocean and performs better than other algorithms, and this result agrees with Jozef et al. (2022). Furthermore, we will explore ways to improve the Ri_b algorithm to make it more suitable for cloudy and convective conditions.
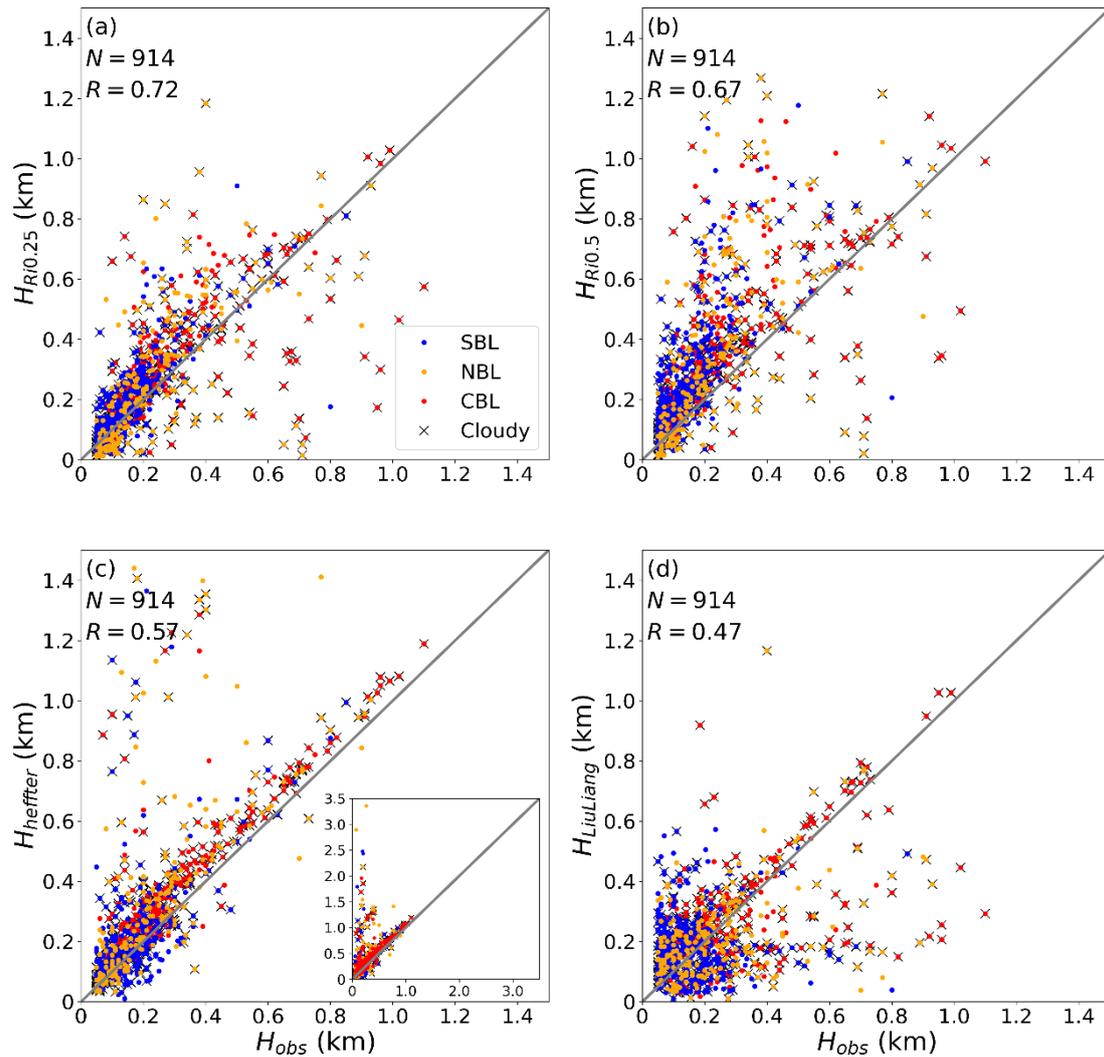
273
274 Figure 3 Comparisons of the ABLHs determined from radiosonde profiles using the bulk Richardson number
275 (Ri_b) algorithm with the critical values (Ri_{bc}) of (a) 0.25 and (b) 0.5, (c) the Heffter algorithm, and (d) the
276 Liu-Liang algorithm with the manually-identified "observed" ABLHs. The blue, yellow, and red colors
277 indicate regime types of SBL, NBL, and CBL, respectively. The "x" signs indicate the Cloudy ABLs. The
278 case numbers (N) and correlation coefficients (R) are given in each panel. The subgraph in (c) denotes all
279 data points ranging from 0 to 3.5 km.

280
281
282
283
284
285
286
287
288

289 Table 1 The statistical measures (*R*, *Bias*, *MEAE*) for the four algorithms applied to the radiosonde dataset.

290 All correlation coefficients are statistically significant ($p < 0.05$), except for SBL types in the Liu-Liang

291 algorithm.

Algorithm	Regime type	R	Bias	MEAE (m)
The Ri_b algorithm with $Ri_{bc} = 0.25$	ALL	0.72	0.10	50
	SBL	0.81	0.16	34
	NBL	0.68	-0.04	62
	CBL	0.65	0.15	71
	Cloudy	0.69	0.08	51
The Ri_b algorithm with $Ri_{bc} = 0.5$	ALL	0.67	0.40	97
	SBL	0.73	0.50	88
	NBL	0.61	0.23	91
	CBL	0.60	0.39	120
	Cloudy	0.66	0.36	94
The Heffter algorithm	ALL	0.57	0.23	53
	SBL	0.46	0.17	33
	NBL	0.45	0.30	59
	CBL	0.66	0.28	74
	Cloudy	0.68	0.25	59
The Liu-Liang algorithm	ALL	0.47	0.04	82
	SBL	0.05	0.15	90
	NBL	0.44	-0.07	81
	CBL	0.56	-0.05	69
	Cloudy	0.52	-0.01	82
The improved Ri algorithm with $Ri_{bc} = 0.35$	ALL	0.85	-0.06	29
	SBL	0.79	-0.08	21
	NBL	0.79	-0.18	35
	CBL	0.87	0.05	36
	Cloudy	0.86	-0.03	30

292

293

3.3 An improved *Ri* algorithm considering the cloud effect

295 As a traditional Ri_b formula, Eq. (3) may break down in cases of ABLs with relatively high wind speed

296 and upper-level stratification due to the overestimation of shear production (Kim and Mahrt, 1992).

297 Vogelezang and Holtslag (1996) proposed a finite-difference *Ri* formula, which is expressed as:

298
$$Ri_F = \frac{(g/\theta_{vs})(\theta_{vh}-\theta_{vs})(h-z_s)}{(u_h-u_s)^2+(v_h-v_s)^2+bu_*^2}, (6)$$

299 where z_s is the lower boundary for the ABL, θ_{vs}, u_s, and v_s are the θ_v and wind components at the height z_s,

300 respectively, b is an empirical coefficient, and u_* is the surface friction velocity. Ri_F is considered for a parcel

301 located somewhat above the surface to avoid the above problem, and u_* is also taken into account to avoid

302 underestimation in the situation of a uniform wind profile in the upper layer. Here, we use Ri_F for clear-sky

303 profiles and take z_s and b values as 40 m and 100, respectively, according to Zhang et al. (2020).

304 As shown in Fig. 3, the estimations of cloudy ABLHs are sometimes quite poor, which motivates us to further

305 improve the algorithm. Under cloudy conditions, the moist Richardson number (Ri_m) can be used to include

306 cloud effects on the buoyancy term. Brooks et al. (2017) adopted the Ri_m formula expressed as:

307
$$Ri_m = \frac{\left(\frac{g}{T}\right)\left(\frac{dT}{dz}+\Gamma_m\right)\left(1+\frac{Lq_s}{RT}\right)-\frac{g}{1+q_w}\frac{dq_w}{dz}}{\frac{du^2}{dz}+\frac{dv^2}{dz}}, (7)$$

308 where T is air temperature, Γ_m is the moist adiabatic lapse rate, L is the latent heat of vaporization, q_s is the

309   saturation mixing ratio, and q_w is the total water mixing ratio, i.e., $q_w=q_s+q_L$, where q_L is the liquid water

310   mixing ratio and is obtained based on the condensed water content. However, Eq. (6) is a gradient Ri and is

311   calculated based on local gradients of wind speed, temperature, and humidity. To be consistent with the Ri

312   formula proposed by Vogelezang and Holtslag (1996), we rewrite the formula in a finite-difference form

313   expressed as:

$$Ri_m=\frac{\left[(g/T_s)\left(\frac{T_h-T_s}{h-z_s}+\Gamma_m\right)\left(1+\frac{Lq_{sh}}{RT_h}\right)-\frac{g}{1+q_{wh}}\frac{q_{wh}-q_{ws}}{h-z_s}\right](h-z_s)^2}{(u_h-u_s)^2+(v_h-v_s)^2+bu_*^2},\ (8)$$

315   where subscripts (h and s) of the variables denote the calculated height, similar to Eq. (6), but note that the

316   s and z_s are adjusted to 130 m, given the cloud radar blind zone. Considering that Ri_m is only appropriate for

317   the liquid-bearing cloud cases, we use the Ri_F for "clear" grid points and use Ri_m for "cloudy" grid cells.

318   Using this improved approach, we evaluated the best value of Ri_c to minimize the errors compared to the

319   reference data set, arriving at an optimal value of $Ri_c=0.35$. The comparison of ABLH estimates obtained

320   through the improved Ri algorithm with the manually-labeled ABLHs demonstrates significant improvement

321   relative to other algorithms, particularly for cloudy conditions (Fig. 4, Table 1).

322   Since some other studies have proposed different Ri_c values for MOSAiC (e.g., Jozef et al., 2022; Barten

323   et al., 2023; Akansu et al., 2023), we will discuss the difference in Ri_c values here. The first thing to make

324   clear is that these studies use different formulas to obtain Ri profiles. Barten et al. (2023) and Akansu et al.

325   (2023) both use the traditional Ri_b algorithm based on Eq. (3), while they used Ri_c values of 0.4 and 0.12,

326   respectively. This difference was likely caused by the different methods to manually derive their reference

327   ABLH data sets. Jozef et al. (2022) calculates the Ri over a rolling 30 m altitude range, labeled as Ri_r, and

328   the criterion is modified to require four consecutive data points to be above the Ri_c of 0.75. In our study, we

329   use Ri_F proposed by Vogelezang and Holtslag (1996) for clear-sky conditions, and Ri_m for cloudy conditions.

330   Based on the results presented here, it is apparent that this more complex approach improves the error

331   statistics relative to approaches based on Eq. (3), regardless of Ri_c. In addition, some of the differences may

332   also related to authors using different data sets or time periods. For instance, Akansu et al. (2023) primarily

333   used sounding data based on tether balloon for a specific sub-period of MOSAiC, and Jozef et al. (2022)

334   used radiosondes from when they had concurrent UAV observations. The data used in our study are based

335   on merged sounding-tower product, as mentioned above.

336   To further explore the differences among the four different approaches, we examine one SBL and CBL

337   case. For a clear-sky SBL case (Fig. 5 a, b), the approaches from Akansu et al., Jozef et al. (2022), and this

338   study all agree closely with the manual ABLH, while the Barten et al. approach results in a significant

339   overestimation. For a cloudy-sky CBL case (Fig. 5 c, d), the approach from this study agrees with the manual

340   ABLH, while the approach from Barten et al. overestimates the ABLH by about 30 m, and the approaches

341   from Akansu et al. and Jozef et al. (2022) underestimate the ABLH by 130 m and 230 m, respectively. These

342   results further demonstrate how Ri_c depends on the choice of Ri formula. Moreover, Ri_c is not analytically

343   derived from basic physical principles (Zilitinkevich et al. 2007), and the concept of Ri_c is challenged by

344   non-steady regimes (Zilitinkevich and Baklanov, 2002) and the hysteresis phenomenon (Banta et al., 2003;

345   Tjernström et al., 2009). Therefore, an objective Ri_c does not exist. Rather, it is empirically used as an

346   algorithmic parameter to simply derive the ABLH.

347
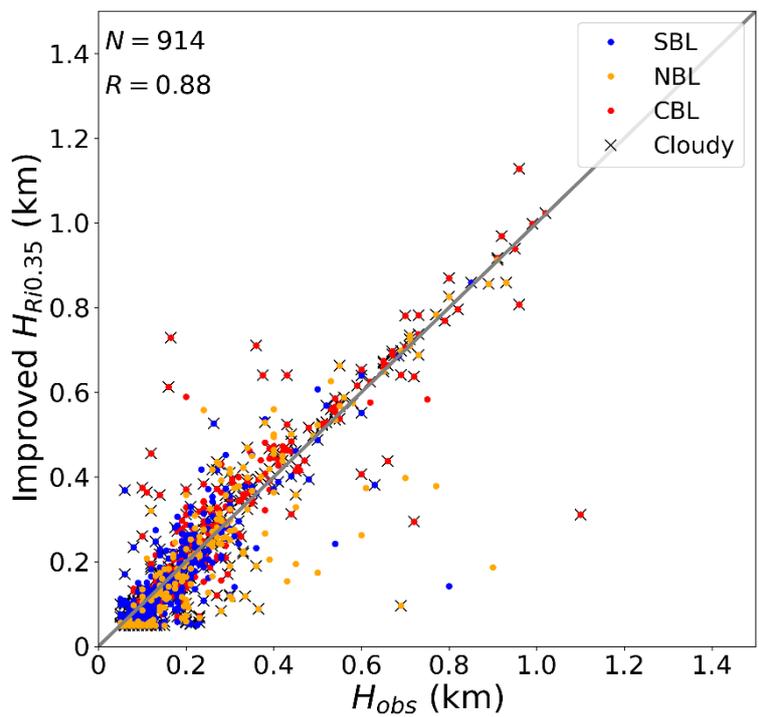
348

349   Figure 4 Similar to Fig. 3, but for the comparison of the ABLHs determined by the improved Ri algorithm

350   with the observed ABLHs. The case number (N) and correlation coefficient (R) are given.

351
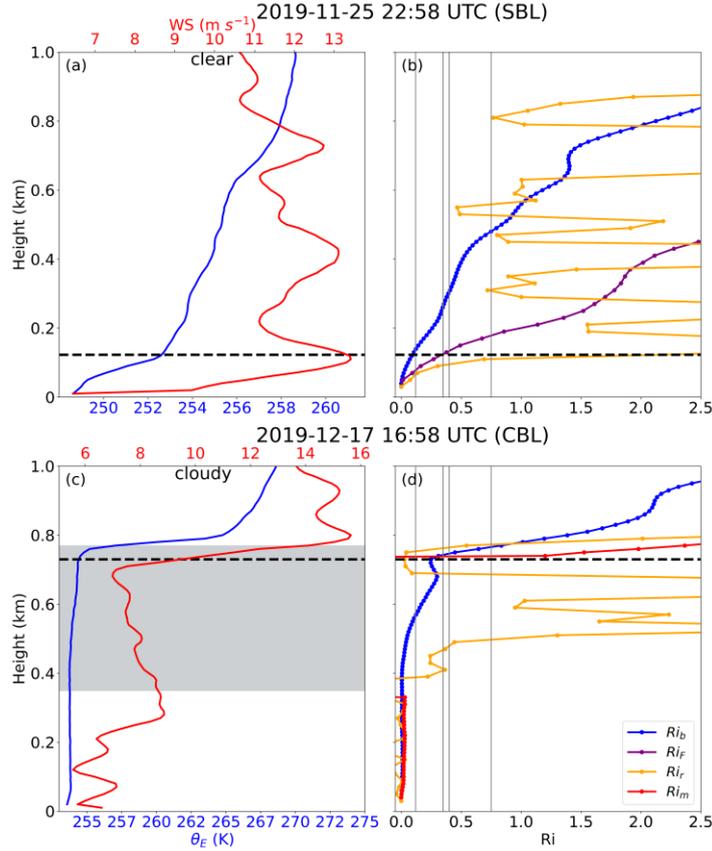
Figure 5 Vertical profiles of (left) θ_E and wind speed, and (right) Ri based on different formulas at (a–b) 25 November 2019, 22:58 UTC and (c–d) 17 December 2019, 16:58 UTC. Boundary layers at the two times represent a clear-sky SBL and a cloudy-sky CBL respectively. The black dashed horizontal lines denote the manually-identified ABLH, and the gray solid vertical lines denote the different Ri_c values, including 0.12, 0.35, 0.4, and 0.75. The gray shading in (c) denotes the cloud layer.

3.4 The stability dependence of critical Richardson number

Richardson et al. (2013) and Basu et al. (2014) suggested that there is a stability dependence of Ri_c in stable conditions, which is different from the constant $Ri_c = 0.35$ used in our improved algorithm. In this section, we will discuss the impact of this dependence on ABLH estimation. We use the improved Ri algorithm to calculate the Ri at the manually-labeled ABLH (h). This new parameter is named Ri_h to distinguish it from the constant Ri_c. To be consistent with Basu et al. (2014), the bulk stability parameter h/L is used for our analysis, where L is the Obukhov length. Based on these two variables, the stability dependence can be expressed as:

$$Ri_h = \alpha \frac{h}{L}, \ (9)$$

where α is a proportionality constant. As suggested in Basu et al. (2014), the data for convective, near-neutral, and very stable conditions are excluded to obtain a credible α. Specifically, data points that meet the thresholds ($L > 500$ m and $L < L_{min}$) are excluded in our analysis, where the L_{min} corresponds to the heat flux minimum (Basu et al. 2008) and is assumed as 20 m here. Finally, we select 168 samples. The Ri_h plotted as

a function of h/L for these selected data is presented in Fig. 6, and the value of L is colored to probe if the dependence is simply due to self-correlation. The results show Ri_h values that mostly range from 0 to 0.75, and the best-fit line indicates an overall positive correlation trend, with $\alpha = 0.11$. The α value is somewhat larger than the results in Richardson et al. (2013) and Basu et al. (2014), which is attributed to the different Ri algorithm used in our study. In addition, if a few of the extreme points are removed, the bulk of the data does not show a strong h/L dependence and is instead fairly well represented by a constant $Ri_h = 0.35$, which is also suitable for convective conditions (e.g., Fig. 5c, d).

In summary, we assess the stability dependence of Ri_c based on our improved Ri algorithm, and the results present an overall positive correlation trend. However, this type of stability dependence of Ri_c is challenged to be used in practical applications because the sensitivity of α to surface characteristics and atmospheric conditions can additionally degrade the accuracy of ABLH estimates. In addition, Eq. (9) requires a priori determination of the ABLH, which also causes difficulties for practical applications of such an approach. Therefore, we still use the Ri algorithm with fixed $Ri_c = 0.35$ for simplicity.
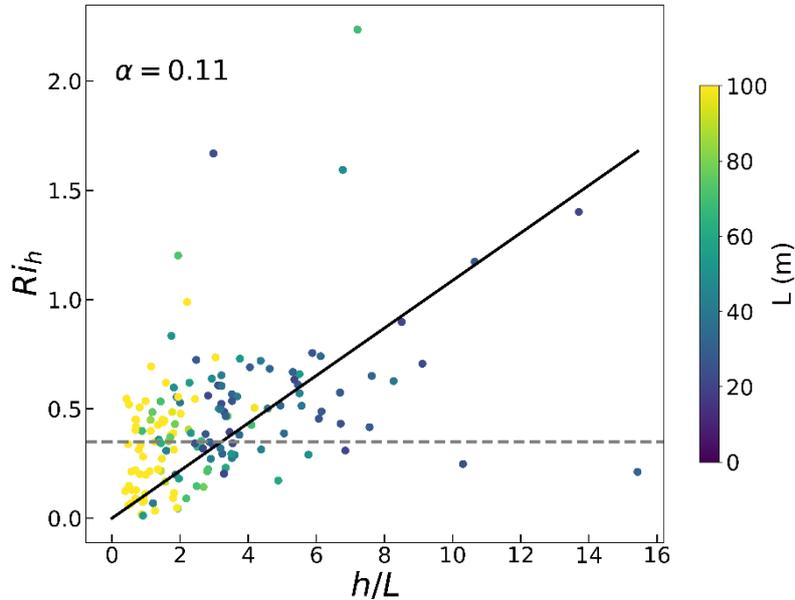
Figure 6 Ri_h versus h/L for selected cases. The data points are colored based on the value of L. The black solid line is the best fit for the selected data points, and the best-fit α value is also given. The gray dashed line is the constant $Ri_c = 0.35$ used in the improved Ri algorithm.

4 MOSAiC ABLH variation and controlling factors

4.1 Overall distribution of ABLH

In this section, we analyze the ABLH variation during the MOSAiC and relevant controlling factors, based on the manually-labeled ABLH dataset and the ABL types that are determined through Eq. (1), or only the θ_E difference if SH is unavailable. The full-time series of ABLH during the MOSAiC expedition is presented in Fig. 7 and forms the basis for the remaining analyses. According to near surface conditions and

the sea ice state, the whole MOSAiC observation period is divided into "freeze up", "winter", "transition", and "summer melt" periods (Shupe et al., 2022), roughly corresponding to the seasons of autumn, winter, spring, and summer, respectively. In Figure 7, the black solid lines indicate persistent low-level clouds that exist for more than 12 h; these occur most frequently in the late summer and autumn (the "freeze up" period), which agrees with Shupe et al. (2011). Note that the grey dots indicate that the ABL data were observed while the vessel was in transit, and the representativity of the ABLH data should be considered in this context. For the first such period, the vessel left the MOSAiC ice floe in mid-May and slowly progressed south through tightly consolidated sea ice, such that the data are generally representative of the sea ice pack in the region. Measurements from early June when the vessel was near or in open water close to Svalbard have been excluded entirely from the analysis. In the middle of June, as the vessel returned to the original MOSAiC ice floe, the sea ice was not as tightly consolidated and the vessel preferentially went through leads; the preferentially lower ice fraction along this transit could have impacted the thermal structure of the ABL. For the three weeks in early August, the vessel moved around in the Fram Strait area and then made its way north to another passive sea ice drifting position near the North Pole, again transiting through regions with lower sea ice fraction. Finally, at the very end of the expedition, the vessel took some time to exit the sea ice, stopping a few times to allow for work on the ice.

Overall, as shown in Fig. 7, the mean ABLH during the whole observation period is 231 m. This is lower than the typical ABLH over the Arctic land surface (Liang and Liu, 2010), which is primarily attributed to the stronger suppression of the temperature inversion over the sea-ice surface. The Arctic ABL is suppressed for most of the MOSAiC year, while for a few periods it intensively develops for several days at a time, most commonly when clouds and a CBL are present. For instance, frequent, intensive ABL development occurs in the "transition" period from 13 April through to 24 May 2020. In this period, the convective thermal structure and cloud effects contribute to ABLH reaching over the 95th percentile of the ABLH data (horizontal dotted line) for about 7 days, with the maximum ABLH of 1100 m. In contrast, the ABL is strongly suppressed in the period from 15 July through to 30 August 2020, with a mean ABLH of only 136 m. The specific mechanisms of ABL development and suppression in these two cases will be analyzed in Sections 4.3 and 4.4, respectively.

Figure 8 presents the frequency distribution of ABLH under SBL, NBL, and CBL regime types. Overall, the sample number of SBL cases is more than that of NBL and CBL cases during the MOSAiC period (43 % for SBL, 31% for NBL, and 26 % for CBL). These occurrence frequencies roughly agree with Jozef et al. (2023), while their results show more NBL and CBL and less SBL. It is likely to be attributed to differences in classification criteria. The distributions of SBL and NBL ABLH are skewed towards small values, with 94 % and 79% of the ABLH values lower than 400 m, and mean values of 165 m and 256 m, respectively. For CBL, the distribution is shifted somewhat towards larger values, with 23 % of the ABLH values higher than 600 m and a mean value of 309 m.
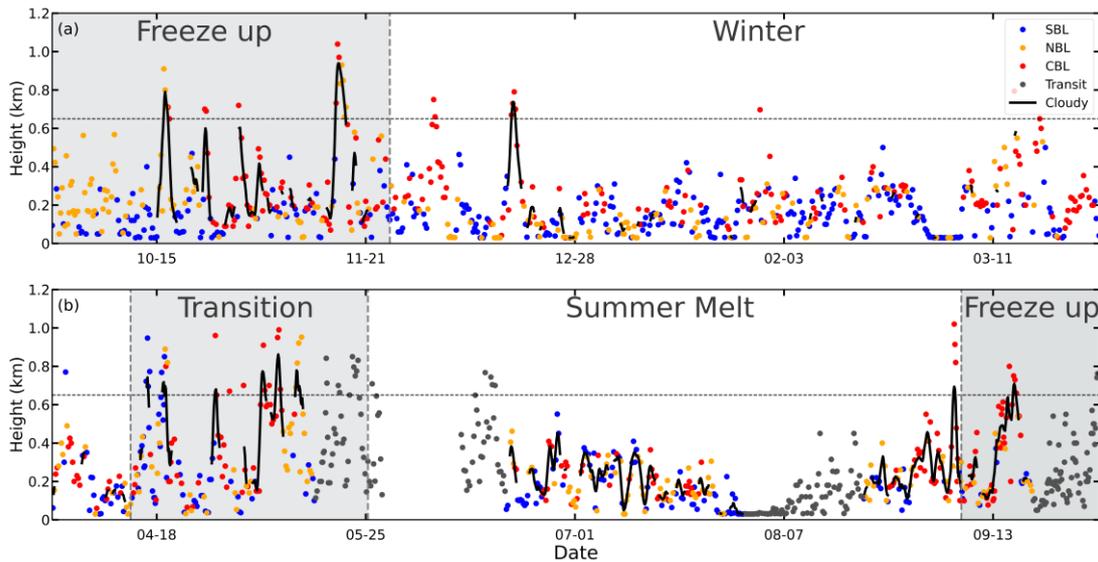
434

435 Figure 7 Time series of ABLHs throughout the MOSAiC year is divided into (a) and (b). The blue, yellow,

436 and red dots indicate the heights of SBL, NBL, and CBL, respectively. The gray dots indicate ABL data

437 observed while the vessel was in transit. The black solid lines indicate the heights of cloudy ABLs and persist

438 for at least 12 hours. The gray dashed horizontal line denotes the 95th percentile of ABLH (650 m). The gray

439 and white background shadings indicate the periods under different surface-melting states, i.e., "freeze up",

440 "winter", "transition", and "summer melt" periods.

441
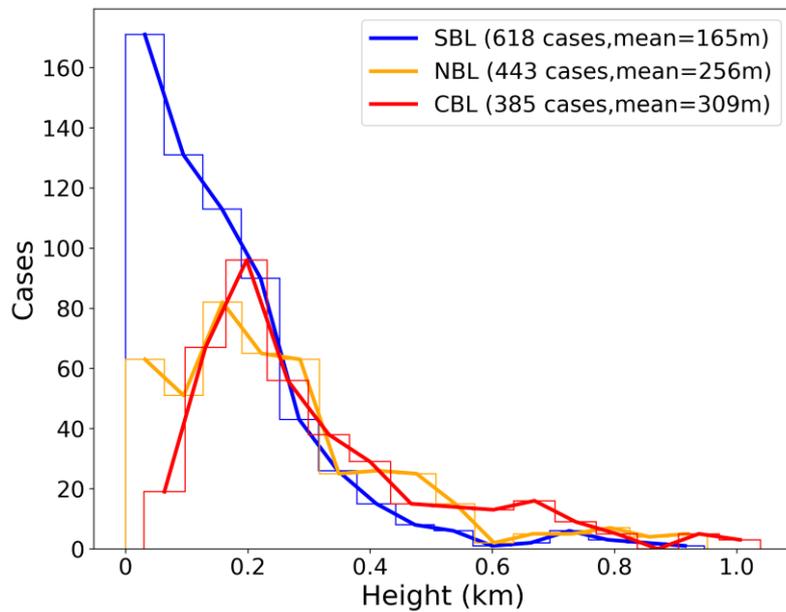
442

443 Figure 8 Frequency distribution of SBL height (blue), NBL height (yellow), and CBL height (red). The case

444 numbers and the mean values of ABLH for SBL, NBL, and CBL conditions are also given.

445

446 **4.2 Annual cycle of ABLH and related factors**

447 Figure 9 presents the annual cycle of monthly ABLH statistics during the MOSAiC expedition in terms

448 of 5th, 25th, 50th, 75th, and 95th percentiles of ABLH (boxplots) and the mean value ("x" signs and solid

and dashed lines). The box-and-whisker plots show a distinct peak in May, with a median value of 363 m and the 95th percentile reaching over 800 m. An abrupt decrease occurs in the following July and August, and another minimum occurs in January, all with median values below 150 m. It should be noted that the ABLH data in transit (gray dots in Fig. 7) are also included in the statistics, which could have potential impact from somewhat more open-water surface conditions. Specifically, the ABLH data during transit periods cause higher mean ABLH for June and lower mean ABLH for August (see Fig. 7). The comparison between cloudy and clear-sky ABLHs indicates that the low-level clouds significantly contribute to the Arctic ABL development during the MOSAiC year, except in winter, when low-level clouds are rare.

The annual cycle of ABLH is determined by the seasonal evolution of the ABL structure (Tjernström et al., 2009; Palo et al., 2017), as revealed through median profiles of θ_E in each month (Fig. 10). The results show that from the start of the MOSAiC expedition (October 2019), the near-surface θ_E gradually decreases due to seasonal surface radiative cooling in the absence of sunlight, more rapidly than the atmosphere cools, which causes a strong surface temperature inversion. The increasing inversion strength through January leads to decreasing ABLH into "winter." In February and March, the surface remains steady while the atmosphere cools more, leading to diminished temperature inversion strength and a small increase in ABLH. After March 2020, with the return of sunlight, the θ_E starts to rise over the whole lower atmosphere, and the near-surface air temperature warms somewhat more than the atmosphere above. This differential warming leads to more frequent near-neutral or convective thermal structures and contributes to high ABLH during the "transition" period. In July and August, the upper-layer temperature continues to rise while the near-surface temperature is constrained to ~0 °C due to the melting sea ice surface, which leads again to a surface inversion and a diminished ABLH during the "summer melt" period. In September, as the sun descends to much lower angles, the θ_E across the whole lower atmosphere starts to drop, with more rapid cooling in the atmosphere relative to the near-surface resulting again in near-neutral or convective thermal structures and an increase in the CBL height during the "freeze up" period. The whole process forms these general shifts over the annual cycle. In addition, we examined the potential implications of the diurnal cycle on the ABL thermal structure. Monthly profiles based on different moments of a day were found to show little variability (not shown), such that the impact of the diurnal cycle is minimal.
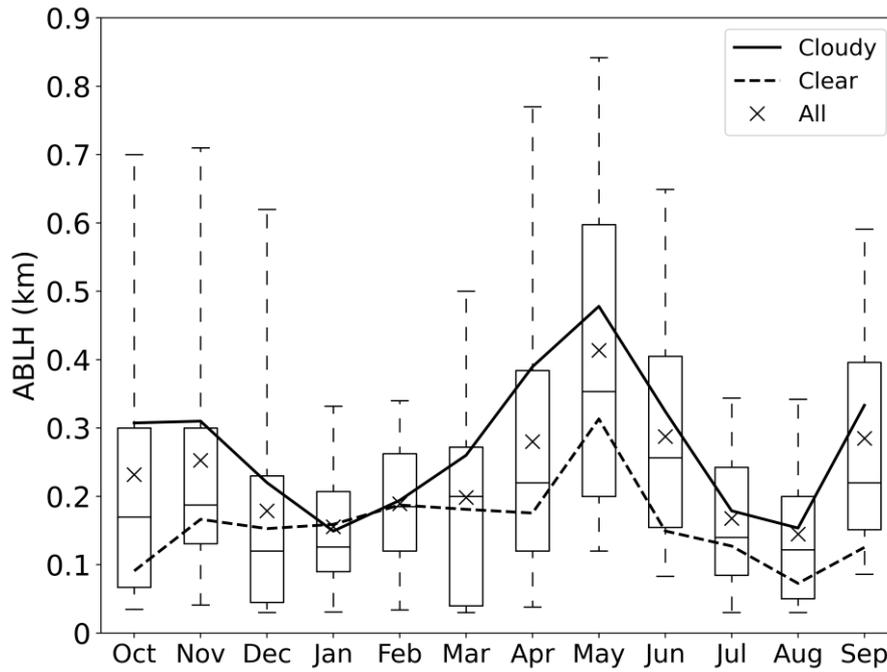
Figure 9 Box-and-whisker plots of the ABLH distribution in each month throughout the MOSAiC year. The whiskers, the boxes, and the black horizontal lines show the 5th, 25th, 50th, 75th, and 95th percentile values of ABLH. The solid and dashed lines and the "x" signs indicate the mean ABLH of cloudy, clear, and all ABL types, respectively.
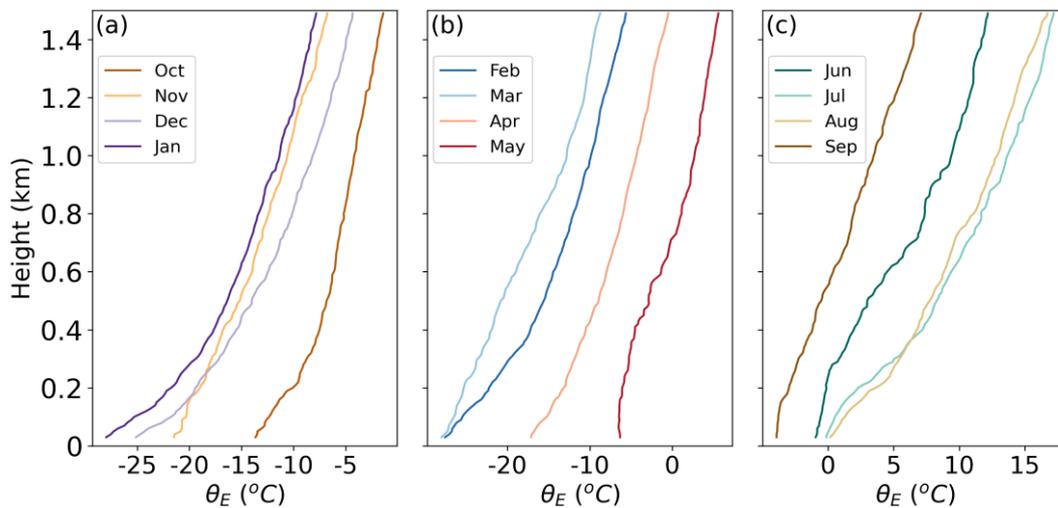
Figure 10 Monthly median profiles of equivalent potential temperature throughout the MOSAiC year are divided into (a), (b), and (c).

To further explore the relations between surface conditions and the ABLH, we evaluate the correlations between the ABLH and three near-surface meteorological and turbulence parameters during the MOSAiC period, including the near-surface equivalent potential temperature gradient ($\theta_{Egrad}=\theta_{E\ 10m}-\theta_{E\ 2m}$), friction velocity ($u_*$), and TKE dissipation rate (ε). The results are shown in Fig. 11. Generally, the near-surface buoyancy and shear effects both modulate these variables. In Fig. 11a, the ABLH distribution for negative

491 θ_{Egrad} has a wide range from the lowest level to above 1 km. As θ_{Egrad} becomes positive and increases, the

492 ABLH distribution rapidly narrows to below 200 m. In general, positive θ_{Egrad} means a stably stratified ABL

493 and surface-based temperature inversion, both of which lead to low ABLH, and negative θ_{Egrad} means that

494 atmospheric stability near the surface is near-neutral or convective, which is necessary for ABL development.

495 The u_* presents a significant correlation with the ABLH, with correlation coefficient of 0.58 (Fig. 11b). High

496 u_* values, which are related to strong mechanical mixing, contribute to the ABL development. However, it

497 is worth noting that intensive ABL development (ABLH over 600 m) only occurs as u_* ranges between 0.2

498 and 0.5 m s^{-1}, which suggests that other factors exist to facilitate further development of the ABL, such as

499 cloud effects (see Fig. 9). The ε is usually a qualitative proxy for turbulence kinetic energy, since higher TKE

500 means larger spectral values at low frequencies, hence higher dissipation rate due to the energy cascade in

501 the inertial subrange. In Fig. 11c, when ε is less than 5×10^{-5} m^2 s^{-3}, turbulence in the ABL is limited with

502 almost all ABLH values below 200 m. As ε increases and becomes larger than 5×10^{-5} m^2 s^{-3}, the average

503 ABLH increases with active turbulent mixing in the ABL. The threshold of 5×10^{-5} m^2 s^{-3} is proposed by

504 Brooks et al. (2017) as the distinction between turbulent and non-turbulent flows.

505 The free-flow stability (characterized by the free-flow Brunt-Väisälä frequency, N) can affect the ABLH

506 (Zilitinkevich et al., 2002; Zilitinkevich and Baklanov, 2002; Zilitinkevich and Esau, 2002, 2003), and

507 therefore is also examined here. Based on the buoyancy flux at the surface (B_s) and N, the NBLs and SBLs

508 can be further divided into four types: the truly neutral (TN, $B_s = 0$ and $N = 0$), the conventionally neutral

509 (CN, $B_s = 0$ and $N > 0$), the nocturnal stable (NS, $B_s < 0$ and $N = 0$), and the long-lived stable boundary layer

510 (LS, $B_s < 0$ and $N > 0$). According to Zilitinkevich and Baklanov (2002), we calculate the N and B_s and

511 reclassify the SBLs and NBLs. We find that the percentages of $N > 0.015$ in SBLs and NBLs are 89 % and

512 80 %, which indicates that LS and CN types dominate the stable and neutral conditions for MOSAiC,

513 respectively. Since only 80 TN cases were identified, these are deemed to be too few for additional analysis

514 of this type. Zilitinkevich and Esau (2003) gave ABLH equations relevant to each ABL type as:

515
$$h_E=\begin{cases}C_Nu_*|fN|^{-1/2} & \text{(Pollard et al., 1973)} & \text{for CN ABL, (10)}\\C_Su_*^2|fB_s|^{-1/2} & \text{(Zilitinkevich, 1972)} & \text{for NS and LS ABL, (11)}\end{cases}$$

516 where h_E is the equilibrium ABLH, f is the Coriolis parameter, and C_N and C_S are empirical coefficients. In

517 addition, Vogelezang and Holtslag (1996) and Steeneveld et al. (2007a) also explore a h_E equation without

518 taking into account f explicitly, expressed as:

519
$$h_E=C_i\frac{u_*}{N} \quad \text{for all SBL and NBL, (12)}$$

520 where C_i is an empirical coefficient. Here we select the CN, NS, and LS ABLH dataset, and fit the data with

521 the corresponding expressions in Eq. (10–12) to obtain the empirical coefficients, and the results are

522 presented in Fig. 12. All three expressions tend to well represent the ABLHs, with significant correlation

523 coefficients. The empirical coefficients C_N and C_S are 1.7 and 0.4, respectively, which are close to the typical

524 values determined through large-eddy simulations (Zilitinkevich, 2012). The coefficient $C_i = 20$ in Fig. 12c

525 is double the typical value of 10 (Vogelezang and Holtslag, 1996), but agrees with the results reported by

526 Overland and Davidson (1992) for the ABL over sea ice. The difference in C_i may be attributed to the unique

527 free-flow stability or other potential mechanisms of ABL development in the Arctic atmosphere.

528   In summary, near-surface conditions and free-flow stability play a key role in ABL development and

529 are also an indicator, in that one can roughly determine the development state of the whole ABL from these

530 basic variables.

531
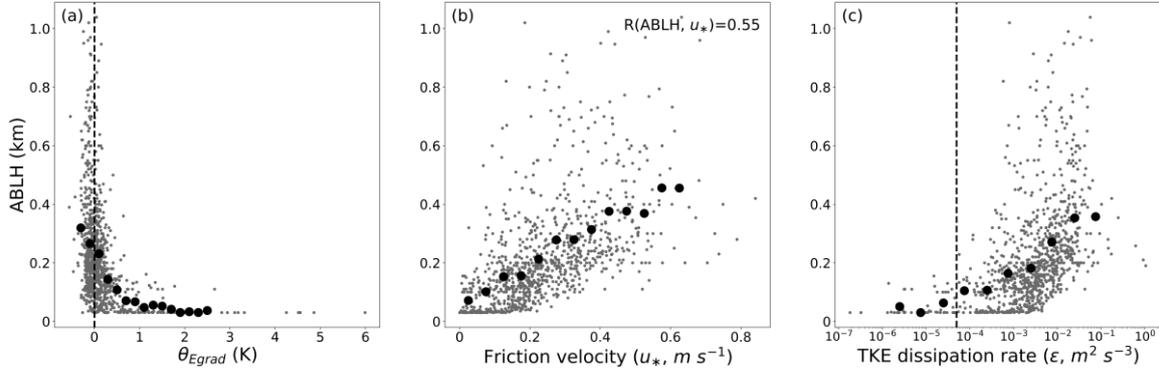
532

533 Figure 11 The ABLHs and bin-averaged values for (a) equivalent potential temperature gradient, θ_{Egrad} (K),

534 (b) friction velocity, u_* (m s^{-1}), and (c) turbulent kinetic energy dissipation rate, ε (m^2 s^{-3}). The average bins

535 for θ_{Egrad}, u_*, and ε logarithm are 0.2 K, 0.05 m s^{-1}, and 0.5 m^2 s^{-3}, respectively. The correlation coefficient

536 R is given in (b), which is statistically significant ($p < 0.05$). The dashed vertical lines indicate the thresholds

537 of (a) $\theta_{Egrad} = 0$ K and (c) $\varepsilon = 5 \times 10^{-5}$ m^2 s^{-3}.

538
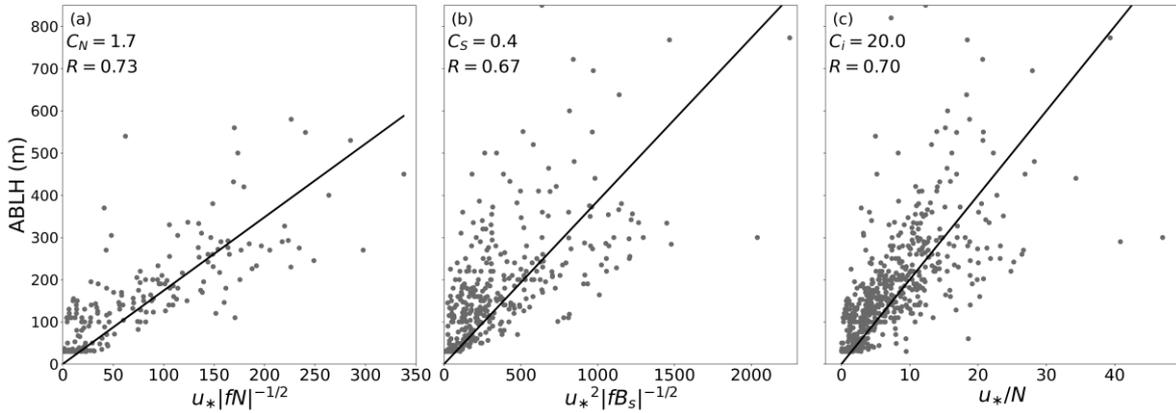
539

540 Figure 12 The ABLHs versus three expressions in Eq. (10–12). The empirical coefficients C_N, C_S, and C_i

541 are given in (a), (b), and (c), respectively, and represent the slope of the best fit line (black line). The

542 correlation coefficient R is given in each panel, which is statistically significant ($p < 0.05$).

543

544 **4.3 Case study #1: Intensively developed ABL 13 April - 24 May 2020**

545   To investigate the unique characteristics of the ABL development and its controlling factors in detail,

546 we analyze the association of the ABLH with vertical thermal structure and near-surface conditions during

547 the transition period (see Fig. 7) when the ABLH was generally the highest. Figure 13 presents time-height

548 cross sections of θ_E, wind speed, and RH, and the time series of near-surface temperature and surface

549 pressure during this period. We divide the whole period into three parts based on the ABLH and the vertical

structure of the lower troposphere. Overall, the near-surface temperature is generally warmer than -20 °C and shows gradual warming towards the melting point. In Period 1, a warm and moist air advection event affects the measurement area, resulting in increased air temperature, near-saturated RH, strong winds throughout the lower troposphere, and low surface pressure. The approximately constant θ_E profile near the surface facilitates exchange between the upper and lower layers, and the high-speed wind profile enhances mechanical mixing, leading to highly developed ABL and ABLH exceeding 600 m. In Period 2, the near-surface air temperature drops again to between -20 and -10 °C, which causes a temperature inversion and partially suppresses the ABL development. However, periodic layers of near-saturated RH extending up to 600m or more indicate the presence of clouds. The ABLH at these times is related to the depth of the near-saturated layer, consistent with a structure where the cloud-induced mixed layer aloft couples with the near-surface mixed layer, forming a deeper ABL and higher ABLH (Wang et al., 2001; Shupe et al., 2013). In Period 3, a high-pressure synoptic system occurs and suppresses the development of the ABL, but the cloud-driven turbulent mixing still exists and counteracts the influence of the high-pressure system. In summary, the development of the ABL mainly depends on large-scale synoptic processes, especially warm-air advection events. Additionally, the interaction between the surface-mixed layer and cloud-mixed layer also plays a significant role in the ABL development.
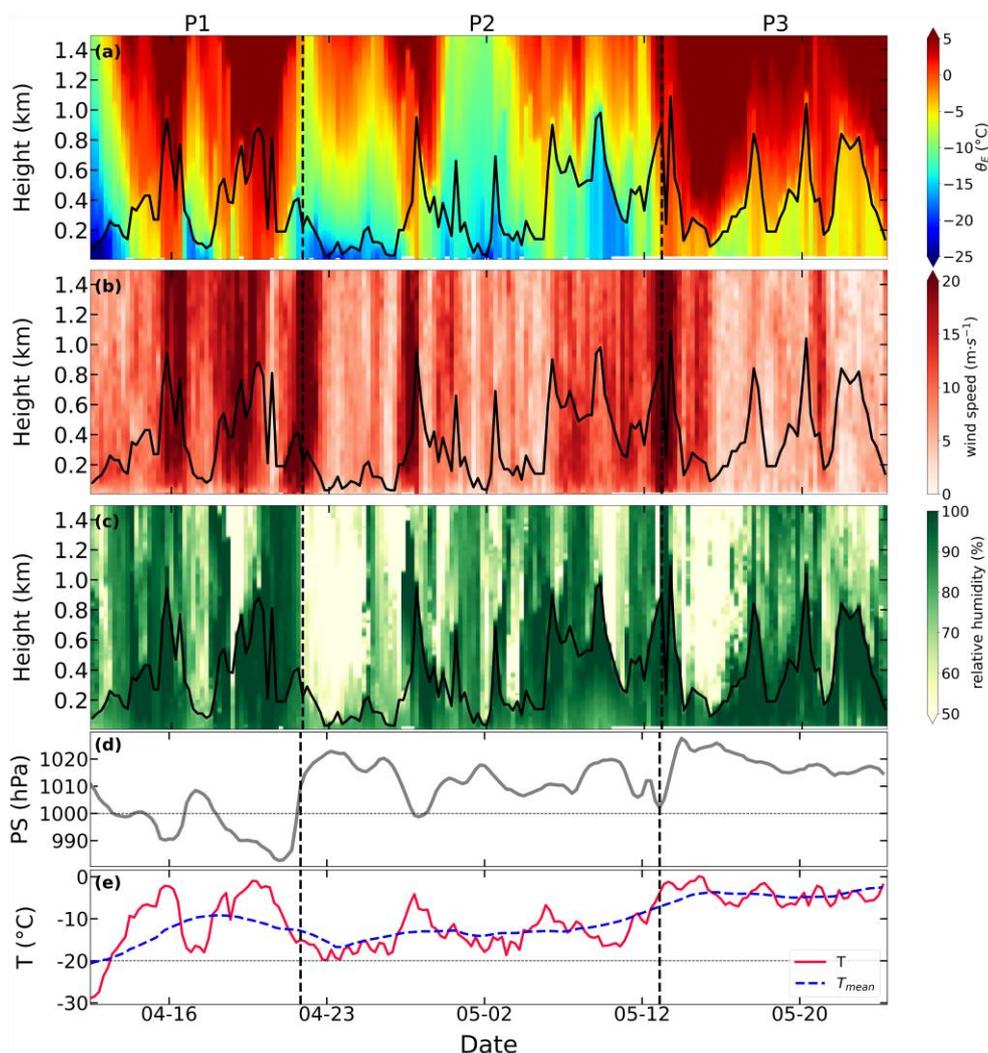
Figure 13 Time-height sections of (a) equivalent potential temperature, (b) horizontal wind speed, and (c) relative humidity and time series of (d) surface pressure and (e) near-surface air temperature (red line) and 7 d running mean of near-surface temperature (blue line). The whole period is from 13 April 2020 to 24 May 2020. Vertical dashed lines mark the identified periods P1 to P3. The black solid lines in panels (a–c) denote the ABLH during this period.

4.4 Case study #2: the severely suppressed ABL 15 July – 30 August 2020

    The Arctic ABL is suppressed most of the time, especially in the late summer for more than a month. We choose the severely suppressed ABL in this period as a case to analyze the influences of vertical thermal structure and near-surface conditions on the ABLH. The results are shown in Fig. 14, and the whole period is divided into three parts, similar to Fig. 13. In Period 1, the near-surface air temperature is constrained to ~0 °C due to the melting surface, and the temperature inversion and weak wind are dominant throughout the lower troposphere, which suppresses the ABL development. In Period 2, warm-air advection occurs in the lower troposphere, strengthening the temperature inversion and contributing to further ABL suppression and an ABLH often lower than 100 m. Because of the constrained near-surface temperature, this structure is distinct from that of the spring "transition" period when warm-air advection facilitates ABL development. In Period 3, the near-surface and upper-layer temperatures start to decrease, and the temperature inversion weakens, which makes the ABLH periodically grow up to ~400 m. Despite that, the ABL is still stably stratified, and the ample moisture and clouds cannot contribute significantly to the ABL development, which is consistent with Shupe et al. (2013). It is important to note that during the second half of Period 2, the *Polarstern* transited from near the sea ice edge to near the North Pole, such that this transition towards weaker temperature inversions is related to both spatial and seasonal shifts. In summary, the suppression of the ABL during the "summer melt" period results from strong temperature inversions and weak winds, and cloud-driven turbulent mixing that is inhibited from interacting with the surface layer due to the near-surface stability. In this period, warm-air advection events enhance the ABL suppression, opposite to the "transition" period.
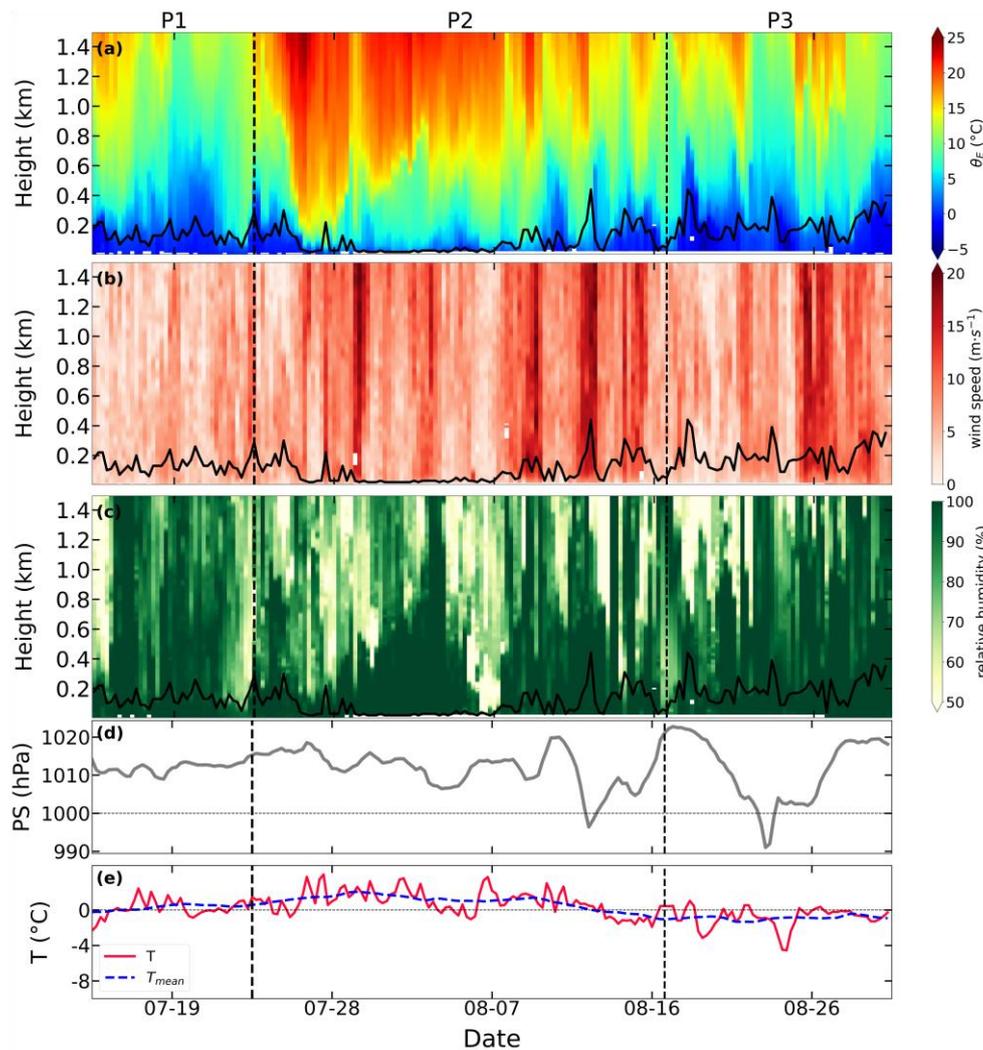
593

594 Figure 14 Similar to Fig. 13, but the period is from 15 July 2020 to 30 August 2020.

595

596

597 **5 MOSAiC – SHEBA comparison**

598   The MOSAiC and SHEBA observations were both made over the Arctic sea ice during yearlong periods.

599 In terms of the location of observation sites, the SHEBA campaign took place in the Beaufort and Chukchi

600 Seas (Perovich et al., 2003), while the MOSAiC observations took place along the transpolar drift for much

601 of the year,in the higher latitudes of the Fram Strait in June, July, and early August, and again near the North

602 Pole in late August and September. The comparison between the two campaigns could provide insight into

603 the spatial and temporal variability in the Arctic ABL structure. The monthly ABLHs of the two campaigns

604 are presented in Fig. 15a. The overall distributions of ABLH are similar during the annual cycle, however,

605 the SHEBA ABLH is significantly higher than the MOSAiC ABLH in June and August. We will discuss

606 these differences based on the ABL thermal structure.

607   Comparisons of monthly θ_E profiles between the two campaigns during June and August are presented

608 in Fig. 15 (b, c). It is clear that θ_E within the lower troposphere during MOSAiC is much higher than that

609 during SHEBA, especially in August. In June, the near-surface θ_E values in both campaigns are close,

because both were over melting sea ice. However, on average, the upper-layer θ_E during SHEBA is lower than that during MOSAiC, especially at a height of around 200 m, which results in decreased low-level stability that supports ABL development. This difference explains why the monthly SHEBA ABLH rises from May to June, but the monthly MOSAiC ABLH decreases at this time. In July at SHEBA, the increased air temperature in the lower troposphere combined with constrained near-surface θ_E results in a significant temperature inversion that suppresses the ABL development (not shown). Thus, the ABLH values at SHEBA and MOSAiC are comparable in July. In August, the θ_E profiles from the two campaigns are significantly different. The surface at both locations is still mostly constrained to be near the melting point, while the lower troposphere at SHEBA starts to cool more than that at MOSAiC. The SHEBA θ_E profile exhibits a near-neutral or convective state, while the MOSAiC θ_E profile shows a further enhanced surface temperature inversion due to warm air advection aloft, which maintains the ABL suppression. To sum up, the increase in air temperature in the lower troposphere in early summer during MOSAiC precedes that during SHEBA, while the cooling of the lower troposphere in late summer during MOSAiC lags that during SHEBA. These are the main factors contributing to the ABLH differences between the two campaigns.

The atmospheric warming during the MOSAiC summer may be attributed to ongoing Arctic warming that contributes a different atmospheric structure, but the impacts of transit periods and different synoptic backgrounds should also be considered. First, there is the complexity of the transit periods during MOSAiC. During the first half of June, *Polarstern* travelled northward into a somewhat loosened sea ice pack and followed open water areas as much as possible. If anything, the higher fraction of open water along this transit path would promote more heat exchange between the surface and ABL and higher ABLH than the regional ice pack (e.g., Fig. 7), which suggests that the observed difference between MOSAiC and SHEBA cannot be explained by this transit period. However, in the first part of August, when *Polarstern* transited preferentially through open water areas during its movement further north, the transit environment was in a persistent melting state with warm air advection aloft. It is not clear how this transit ultimately impacted the monthly ABLH results, although the values during the transit period were lower than those during the final 10 days of August when *Polarstern* was again passively drifting with the sea ice (Figs. 7, 14). Thus, some of the difference from SHEBA at this time could have been attributed to the specific conditions encountered during movement of the vessel. Additionally, these two campaigns were in different storm tracks with markedly different types of regional advection patterns. For example, in summer, MOSAiC was approaching the Fram Strait where northward warm air advection is common. Thus, synoptic variability likely plays a big role in the ABL thermal structure. In summary, there is large variability in the Arctic ABL structure during summer caused by the surface melting state, and more detailed assessments are needed to study the specific causes for the atmospheric warming and possible influences of changing Arctic conditions on the ABL structure.
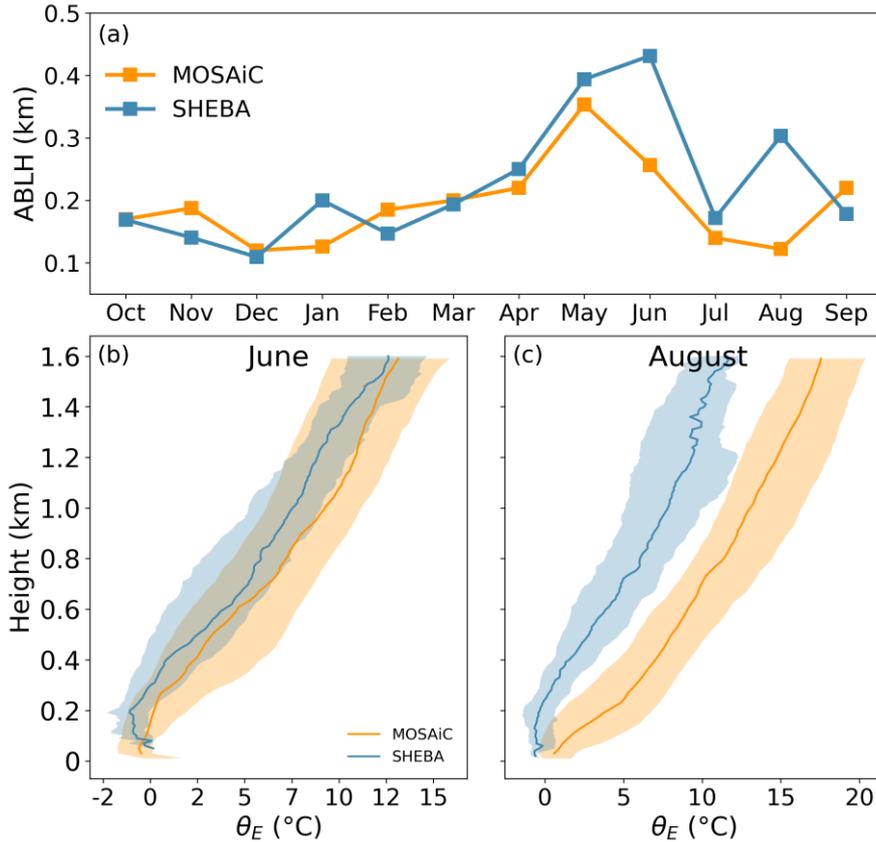
Figure 15 Comparison of ABL during SHEBA (blue squares, lines, and shadings) and MOSAiC (yellow squares, lines, and shadings), including (a) annual cycle of monthly median ABLH and monthly θ_E profiles in (b) June and (c) August. The solid lines in (b–c) indicate the median profiles, and the shadings indicate the range of 25th- and 75th- percentile profiles. The median ABLHs of SHEBA are from Dai et al. (2011).

6 Conclusions

This study is carried out using merged radiosounding data and corresponding surface meteorological observations and cloud properties collected during the MOSAiC expedition over a year-long period. A number of ABLH algorithms are first evaluated, prompting us to implement an improved Ri algorithm that takes cloud effects into consideration. We propose a critical $Ri = 0.35$ and further analyze its value choice and stability dependence. Subsequently, we use the manually-labeled ABLH dataset to study how atmospheric thermal structure and near-surface conditions impact the characteristics and evolution of the ABL during the MOSAiC year. Lastly, we use two cases to explore the mechanisms of ABL development and suppression over the Arctic sea-ice surface. The main conclusions are as follows.

During the MOSAiC year, the mean ABLH is 231 m, with SBLs, NBLs and CBLs accounting for 43 %, 31 %, and 26 % of the profiles, respectively. The annual cycle of the Arctic ABLH is clearly characterized by a distinct peak in May and two minima in January and July-August. L ow-level clouds significantly contribute to the Arctic ABL development during the MOSAiC year, except in winter, when low-level clouds are less frequent. Compared to the SHEBA ABLH, the MOSAiC ABLH is suppressed in June and August, which is caused by increased atmospheric warming in the MOSAiC ABL during the "summer melt" period

665 compared to SHEBA.

666 The annual cycle of ABLH over the Arctic Ocean is primarily controlled by the seasonal evolution of
667 the ABL thermal structure and near-surface meteorological conditions. In the "winter" period, temperature
668 inversions form due to negative net radiation at the surface and are associated with low ABLHs. In the spring
669 "transition" period, the rapid increase of near-surface temperature weakens the temperature inversion,
670 facilitating the development of the ABL. In the "summer melt" period, temperature inversions result from a
671 fixed surface temperature at the melting point and warm-air advection aloft, which suppresses ABL
672 development. For near-surface conditions and free-flow stability, a negative θ_{Egrad} and large TKE dissipation
673 rate are characteristic of significant ABL development. In addition, empirical formulas relating ABLH to
674 friction velocity, near-surface and free-flow stabilities are also tested, and the results suggest that the
675 MOSAiC ABLH can be roughly estimated based on these basic variables.

676 During MOSAiC, the development of the ABL is irregular, and only occurs during intermittent periods.
677 The year is characterized by occasions of abrupt growth of the ABLH and intensive ABLH variation for
678 several days thereafter. These unique features are caused by large-scale synoptic processes (e.g., advection
679 events) that bring heat, moisture, and clouds. It is worth noting that some large-scale events can have the
680 opposite effect on the ABL. For example, warm-air advection can facilitate ABL development in the spring
681 "transition" period but can cause ABL suppression in the "summer melt" period, when the constrained near-
682 surface temperature cannot respond to the warmth aloft.

683 The findings reported here provide new insight into the annual variability and properties of the ABL
684 and ABLH over sea ice in the 'new Arctic.'. The ABLH contains information directly related to the thermal
685 structure of the ABL and includes the impacts of weather events and large-scale circulations on the ABL
686 structure. The ABL development supported by cloud processes was captured by the improved *Ri* algorithm,
687 which is similar to Brooks et al. (2017). However, the representativity of these results must still be
688 established by comparing them with additional observations, and the influences of other variables (e.g.,
689 energy budget terms) on the ABLH should also be considered in future research.

690

Data Availability

692 The radiosonde data are available at the PANGAEA Data Publisher at
693 https://doi.org/10.1594/PANGAEA.943870 (Maturilli et al., 2022). All value-added products and surface
694 meteorological data are available at the archive of the US Department of Energy Atmospheric Radiation
695 Measurement Program. The Planetary Boundary Layer Height Value-Added Product is available at
696 http://dx.doi.org/10.5439/1150253 (Riihimaki et al., 2019). The cloud property data is available at
697 https://doi.org/10.5439/1871015 (Shupe, 2022). The MOSAiC surface flux and other meteorological data
698 are available at the Arctic Data Center at http://dx.doi.org/10.18739/A2PV6B83F (Cox et al., 2023). The
699 merged sounding-tower data are available at PANGAEA. The SHEBA-based sounding data are available at
700 https://doi.org/10.5065/D6FQ9V0Z (Moritz, 2017).

701

Acknowledgments

703 Data used in this manuscript were produced as part of the international Multidisciplinary drifting
704 Observatory for the Study of Arctic Climate (MOSAiC) expedition with tag MOSAiC20192020. We thank
705 all persons involved in the expedition of the Research Vessel Polarstern during MOSAiC in 2019-2020
706 (AWI_PS122_00) as listed in Nixdorf et al. (2021). A subset of data was obtained from the Atmospheric
707 Radiation Measurement (ARM) User Facility, a US Department of Energy (DOE) Office of Science User

Facility Managed by the Biological and Environmental Research Program. The Alfred Wegener Institute, DOE ARM Program, and German Weather Service are acknowledged for their contributions to the MOSAiC sounding program.

Financial Support

This study is supported by the National Natural Science Foundation of China (Nos. 42105072, 41922044, 41941009), the Guangdong Basic and Applied Basic Research Foundation (Nos. 2021A1515012209, 2020B1515020025), and the China Postdoctoral Science Foundation (Nos. 2021M693585). MDS was supported by the US National Science Foundation (OPP-1724551), the DOE Atmospheric System Research Program (DE-SC0019251, DE-SC0023036), and the National Oceanic and Atmospheric Administration Global Ocean Monitoring and Observing program (FundRef https://doi.org/10.13039/100018302, NA22OAR4320151).

References

Akansu, E. F., Dahlke, S., Siebert, H., and Wendisch, M.: Determining the surface mixing layer height of the Arctic atmospheric boundary layer during polar night in cloudless and cloudy conditions, EGUsphere [preprint], https://doi.org/10.5194/egusphere-2023-629, 2023.

Andreas, E. L., Claffy, K. J., and Makshtas, A. P.: Low-level atmospheric jets and inversions over the western Weddell Sea, Boundary-Layer Meteorol., 97, 459-486, https://doi.org/10.1023/A:1002793831076, 2000.

Banta, R. M., Pichugina, Y. L., and Newsom, R. K.: Relationship between low-level jet properties and turbulence kinetic energy in the nocturnal stable boundary layer, J. Atmos. Sci., 60, 2549-2555, https://doi.org/10.1175/1520-0469(2003)060<2549:RBLJPA>2.0.CO;2, 2003.

Barten, J. G. M., Ganzeveld, L. N., Steeneveld, G. J., Blomquist, B. W., Angot, H., Archer, S. D., Bariteau, L., Beck, I., Boyer, M., von der Gathen, P., Helmig, D., Howard, D., Hueber, J., Jacobi, H.-W., Jokinen, T., Laurila, T., Posman, K. M., Quéléver, L., Schmale, J., Shupe, M. D., and Krol, M. C.: Low ozone dry deposition rates to sea ice during the MOSAiC field campaign: Implications for the Arctic boundary layer ozone budget, Elementa: Sci. Anthrop., 11, 00086, https://doi.org/10.1525/elementa.2022.00086, 2023.

Basu, S., Holtslag, A. A. M., Caporaso, L., Riccio, A., and Steeneveld, G. J.: Observational Support for the Stability Dependence of the Bulk Richardson Number Across the Stable Boundary Layer. Boundary-Layer Meteorol. 150, 515–523, https://doi.org/10.1007/s10546-013-9878-y, 2014.

Basu, S, Holtslag, A. A. M., van de Wiel, B. J. H., Moene, A. F., and Steeneveld, G. J.: An inconvenient "truth" about using sensible heat flux as a surface boundary condition in models under stably stratified regimes. Acta Geophys., 56, 88–99, https://doi.org/10.2478/s11600-007-0038-y, 2008.

Blunden, J. and Arndt, D. S.: A Look at 2018: Takeaway Points from the State of the Climate Supplement, Bull. Amer. Meteorol. Soc., 100, 1625-1636, https://doi.org/10.1175/bams-d-19-0193.1, 2019.

Brooks, I. M., Tjernström, M., Persson, P. O. G., Shupe, M. D., Atkinson, R. A., Canut, G., Birch, C. E., Mauritsen, T., Sedlar, J., and Brooks, B. J.: The Turbulent Structure of the Arctic Summer Boundary Layer During The Arctic Summer Cloud-Ocean Study, J. Geophys. Res.-Atmos., 122, 9685-9704, https://doi.org/10.1002/2017jd027234, 2017.

Busch, N., Ebel, U., Kraus, H., and Schaller, E.: The structure of the subpolar inversion-capped ABL, Archives for meteorology, geophysics, and bioclimatology, Series A, 31, 1-18, https://doi.org/10.1007/BF02257738, 1982.

Cox, C., Gallagher, M., Shupe, M., Persson, O., Blomquist, B., Grachev, A., Riihimaki, L., Kutchenreiter, M., Morris, V., Solomon, A., Brooks, I., Costa, D., Gottas, D., Hutchings, J., Osborn, J., Morris, S., Preusser, A., Uttal, T.: Met City meteorological and surface flux measurements (Level 3 Final), Multidisciplinary drifting Observatory for the Study of Arctic Climate (MOSAiC), central Artic, October 2019 - September 2020 [data set], https://doi.org/10.18739/A2PV6B83F, 2023.

Dai, C., Gao, Z., Wang, Q., and Cheng, G.: Analysis of Atmospheric Boundary Layer Height Characteristics over the Arctic Ocean Using the Aircraft and GPS Soundings, Atmospheric Ocean. Sci., 4, 124-130, https://doi.org/10.1080/16742834.2011.11446916, 2011.

Dai, C., Wang, Q., Kalogiros, J. A., Lenschow, D. H., Gao, Z., and Zhou, M.: Determining Boundary-Layer Height from Aircraft Measurements, Boundary-Layer Meteorol., 152, 277-302, https://doi.org/10.1007/s10546-014-9929-z, 2014.

Davy, R. and Esau, I.: Differences in the efficacy of climate forcings explained by variations in atmospheric boundary layer depth, Nat. Commun., 7, 11690, https://doi.org/10.1175/BAMS-D-11-00187.1, 2013.

Esau, I., Pettersson, L. H., Cancet, M., Chapron, B., Chernokulsky, A., Donlon, C., Sizov, O., Soromotin, A., and Johannesen, J. A.: The Arctic Amplification and Its Impact: A Synthesis through Satellite Observations, Remote Sens., 15, 1354, https://doi.org/10.3390/rs15051354, 2023.

Francis, J. A. and Hunter, E.: New insight into the disappearing Arctic sea ice, EOS Trans. Am. Geophys. Union, 87, 509-511, https://doi.org/10.1029/2006EO460001, 2006.

Graversen, R. G., Mauritsen, T., Tjernström, M., Kallen, E., and Svensson, G.: Vertical structure of recent Arctic warming, Nature, 451, 53-U54, https://doi.org/10.1038/nature06502, 2008.

Heffter, J. L.: Transport layer depth calculations., Second Joint Conference on Applications of Air Pollution Meteorology, 1980.

Holtslag, A.A.M., Svensson, G., Baas, P., Basu, S., Beare, B., Beljaars, A.C.M., Bosveld, F.C., Cuxart, J., Lindvall, J., Steeneveld, G.J., Tjernström, M. and Van De Wiel, B.J.H.: Stable atmospheric boundary layers and diurnal cycles: Challenges for weather and climate models, Bull. Amer. Meteorol. Soc., 94, 1691–1706, https://doi.org/10.1038/ncomms11690, 2013.

Jozef, G., Cassano, J., Dahlke, S., and de Boer, G.: Testing the efficacy of atmospheric boundary layer height detection algorithms using uncrewed aircraft system data from MOSAiC, Atmos. Meas. Tech., 15, 4001-4022, https://doi.org/10.5194/amt-15-4001-2022, 2022.

Jozef, G. C., Cassano, J. J., Dahlke, S., Dice, M., Cox, C. J., and de Boer, G.: An Overview of the Vertical Structure of the Atmospheric Boundary Layer in the Central Arctic during MOSAiC, EGUsphere [preprint], https://doi.org/10.5194/egusphere-2023-780, 2023.

Kim, J. and Mahrt, L.: Simple Formulation of Turbulent Mixing in the Stable Free Atmosphere and Nocturnal Boundary Layer, Tellus, 44A, 381-39, https://doi.org/10.3402/tellusa.v44i5.14969, 1992.

Kljun, N., Calanca, P., Rotach, M. W., and Schmid, H. P.: The simple two-dimensional parameterisation for Flux Footprint Predictions (FFP), Geosci. Model Dev., 8(8), 6757–6808, https://doi.org/10.5194/gmd-8-3695-2015, 2015.

Knudsen, E. M., Heinold, B., Dahlke, S., Bozem, H., Crewell, S., Gorodetskaya, I. V., Heygster, G., Kunkel, D., Maturilli, M., Mech, M., Viceto, C., Rinke, A., Schmithusen, H., Ehrlich, A., Macke, A., Luepkes, C., and Wendisch, M.: Meteorological conditions during the ACLOUD/PASCAL field campaign near Svalbard in early summer 2017, Atmospheric Chem. Phys., 18, 17995-18022, https://doi.org/10.5194/acp-18-17995-2018, 2018.

Knust, R.: Polar Research and Supply Vessel POLARSTERN operated by the Alfred-Wegener-Institute, Journal of large-scale research facilities JLSRF, 3, https://doi.org/10.17815/jlsrf-3-163, 2017.

Konor, C. S., Boezio, G. C., Mechoso, C. R., and Arakawa, A.: Parameterization of PBL Processes in an Atmospheric General Circulation Model: Description and Preliminary Assessment, Mon. Weather Rev., 137, 1061-1082, https://doi.org/10.1175/2008mwr2464.1, 2009.

Landrum, L. and Holland, M. M.: Extremes become routine in an emerging new Arctic, Nature Clim. Change, 10, 1108-1115, https://doi.org/10.1038/s41558-020-0892-z, 2020.

Lenschow D. H., Zhou M., Zeng X., Chen L., and Xu X.: Measurements of fine-scale structure at the top of marine stratocumulus, Boundary-Layer Meteorol., 97:331–357, https://doi.org/10.1023/A:1002780019748, 2000.

Liang, X.-Z. and Liu, S.: Observed Diurnal Cycle Climatology of Planetary Boundary Layer Height, J. Clim., 23, 5790-5809, https://doi.org/10.1175/2010jcli3552.1, 2010.

Mahrt, L.: Modelling the depth of the stable boundary-layer, Boundary-Layer Meteorol., 21, 3-19, https://doi.org/10.1007/BF00119363, 1981.

Mahrt, L.: Stably stratified atmospheric boundary layers, Annu. Rev. Fluid Mech., 46, 23–45, https://doi.org/10.1146/annurev-fluid-010313-141354, 2014.

Mahrt L., Heald R. C., Lenschow D. H., Stankov B. B., and Troen I. B.: An observational study of the structure of the nocturnal boundary layer, Boundary-Layer Meteorol., 17:247–264, https://doi.org/10.1007/BF00117983, 1979.

Marsik, F. J., Fischer, K. W., McDonald, T. D., and Samson, P. J.: Comparison of Methods for Estimating Mixing Height Used during the 1992 Atlanta Field Intensive, J. Appl. Meteorol. Climatol., 34, 1802-1814, https://doi.org/10.1175/1520-0450(1995)034<1802:Comfem>2.0.Co;2, 1995.

Martucci G, Matthey R, and Mitev V.: Comparison between backscatter lidar and radiosonde measurements of the diurnal and nocturnal stratification in the lower troposphere, J. Atmos. Oceanic Technol., 24:1231–1244, https://doi.org/10.1175/JTECH2036.1, 2007.

Maturilli, M., Sommer, M., Holdridge, D. J., Dahlke, S., Graeser, J., Sommerfeld, A., Jaiser, R., Deckelmann, H., and Schulz, A.: MOSAiC radiosonde data (level 3) [data set], https://doi.org/10.1594/PANGAEA.943870, 2022.

Matveeva, T. A. and Semenov, V. A.: Regional Features of the Arctic Sea Ice Area Changes in 2000–2019 versus 1979–1999 Periods, Atmosphere, 13, 1434. https://doi.org/10.3390/atmos1309143, 2022.

Meier, W. N., and Stroeve, J.: An updated assessment of the changing Arctic sea ice cover, Oceanography, 35(3–4): 10–19, https://doi.org/10.5670/oceanog.2022.114, 2022.

Moritz, R.: Soundings, Ice Camp NCAR/GLAS raobs. (ASCII). Version 2.0., University of Washington, UCAR/NCAR - Earth Observing Laboratory [data set], https://doi.org/10.5065/D6FQ9V0Z, 2017.

Nixdorf, U., Dethloff, K., Rex, M., Shupe, M., Sommerfeld, A., Perovich, D. K., Nicolaus, M., Heuze, C., Rabe, B., Loose, B., Damm, E., Gradinger, R., Fong, A., Maslowski, W., Rinke, A., Kwok, R., Spreen, G., Wendisch, M., Herber, A., Hirsekorn, M., Mohaupt, V., Frickenhaus, S., Immerz, A., Weiss-Tuider, K., Koenig, B., Mengedoht, D., Regnery, J., Gerchow, P., Ransby, D., Krumpen, T., Morgenstern, A., Haas, C., Kanzow, T., Rack, F., Saitzev, V., Sokolov, V., Makarov, A., Schwarze, S., Wunderlick, T., Wurr, K., Boetius, A.: MOSAiC extended acknowledgement., Zenodo., http://dx.doi.org/10.5281/zenodo.5541624, 2021.

Overland, J. E., Dunlea, E. J., Box, J. E., Corell, R. W., Forsius, M., Kattsov, V. M., Olsen, M. S., Pawlak, J., Reiersen, L. O., and Wang, M.: The urgency of Arctic change, Polar Sci., 21, 6-13, https://doi.org/10.1016/j.polar.2018.11.008, 2019.

Palo, T., Vihma, T., Jaagus, J., and Jakobson, E.: Observations of temperature inversions over central Arctic sea ice in summer, Q. J. R. Meteorol. Soc., 143, 2741-2754, https://doi.org/10.1002/qj.3123, 2017.

Perovich, D. K., Grenfell, T. C., Richter-Menge, J. A., Light, B., Tucker III, W. B., and Eicken, H.: Thin and thinner: Sea ice mass balance measurements during SHEBA, J. Geophys. Res.-Oceans, 108, https://doi.org/10.1029/2001JC001079, 2003.

Persson, P. O. G., Fairall, C. W., Andreas, E. L., Guest, P. S., and Perovich, D. K.: Measurements near the Atmospheric Surface Flux Group tower at SHEBA: Near-surface conditions and surface energy budget, J. Geophys. Res.-Oceans, 107, 35, https://doi.org/10.1029/2000jc000705, 2002.

Pollard R. T., Rhines P.B., and Thompson R.: The deepening of the wind-mixed layer, Geophys. Fluid Dyn., 3, 381–404, https://doi.org/10.1080/03091927208236105, 1973.

Richardson, H., Basu, S., and Holtslag, A. A. M.: Improving Stable Boundary-Layer Height Estimation Using a Stability-Dependent Critical Bulk Richardson Number, Boundary-Layer Meteorol., 148, 93-109, https://doi.org/10.1007/s10546-013-9812-3, 2013.

Riihimaki, L., Sivaraman, C., and Zhang, D.: Planetary Boundary Layer Height (PBLHTSONDE1MCFARL), Atmospheric Radiation Measurement (ARM) User Facility [data set], https://doi.org/10.5439/1150253, 2019.

Seibert, P., Beyrich, F., Gryning, S. E., Joffre, S., Rasmussen, A., and Tercier, P.: Review and

intercomparison of operational methods for the determination of the mixing height, Atmos. Environ., 34, 1001-1027, https://doi.org/10.1016/s1352-2310(99)00349-0, 2000.

Seidel, D. J., Ao, C. O., and Li, K.: Estimating climatological planetary boundary layer heights from radiosonde observations: Comparison of methods and uncertainty analysis, J. Geophys. Res.-Atmos., 115, https://doi.org/10.1029/2009JD013680, 2010.

Seidel, D. J., Zhang, Y. H., Beljaars, A., Golaz, J. C., Jacobson, A. R., and Medeiros, B.: Climatology of the planetary boundary layer over the continental United States and Europe, J. Geophys. Res.-Atmos., 117, 15, https://doi.org/10.1029/2012jd018143, 2012.

Shupe, M. D.: ShupeTurner cloud microphysics product, ARM Mobile Facility (MOS) MOSAiC (Drifting Obs – Study of Arctic Climate) [data set], https://doi.org/10.5439/1871015, 2022.

Shupe, M. D., and Intrieri, J. M.: Cloud radiative forcing of the Arctic surface: The influence of cloud properties, surface albedo, and solar zenith angle, J. Climate, 17, 616–628, https://doi.org/10.1175/1520-0442(2004)017<0616:CRFOTA>2.0.CO;2, 2004.

Shupe, M. D., Walden, V. P., Eloranta, E., Uttal, T., Campbell, J. R., Starkweather, S. M., and Shiobara, M.: Clouds at Arctic Atmospheric Observatories. Part I: Occurrence and Macrophysical Properties, J. Appl. Meteorol. Clim., 50, 626-644, https://doi.org/10.1175/2010JAMC2467.1, 2011.

Shupe, M. D., Persson, P. O. G., Brooks, I. M., Tjernström, M., Sedlar, J., Mauritsen, T., Sjogren, S., and Leck, C.: Cloud and boundary layer interactions over the Arctic sea ice in late summer, Atmos. Chem. Phys., 13, 9379-9399, https://doi.org/10.5194/acp-13-9379-2013, 2013.

Shupe, M. D., Rex, M., Blomquist, B., Persson, P. O. G., Schmale, J., Uttal, T., Althausen, D., Angot, H., Archer, S., Bariteau, L., Beck, I., Bilberry, J., Bucci, S., Buck, C., Boyer, M., Brasseur, Z., Brooks, I. M., Calmer, R., Cassano, J., Castro, V., Chu, D., Costa, D., Cox, C. J., Creamean, J., Crewell, S., Dahlke, S., Damm, E., de Boer, G., Deckelmann, H., Dethloff, K., Dütsch, M., Ebell, K., Ehrlich, A., Ellis, J., Engelmann, R., Fong, A. A., Frey, M. M., Gallagher, M. R., Ganzeveld, L., Gradinger, R., Graeser, J., Greenamyer, V., Griesche, H., Griffiths, S., Hamilton, J., Heinemann, G., Helmig, D., Herber, A., Heuzé, C., Hofer, J., Houchens, T., Howard, D., Inoue, J., Jacobi, H.-W., Jaiser, R., Jokinen, T., Jourdan, O., Jozef, G., King, W., Kirchgaessner, A., Klingebiel, M., Krassovski, M., Krumpen, T., Lampert, A., Landing, W., Laurila, T., Lawrence, D., Lonardi, M., Loose, B., Lüpkes, C., Maahn, M., Macke, A., Maslowski, W., Marsay, C., Maturilli, M., Mech, M., Morris, S., Moser, M., Nicolaus, M., Ortega, P., Osborn, J., Pätzold, F., Perovich, D. K., Petäjä, T., Pilz, C., Pirazzini, R., Posman, K., Powers, H., Pratt, K. A., Preußer, A., Quéléver, L., Radenz, M., Rabe, B., Rinke, A., Sachs, T., Schulz, A., Siebert, H., Silva, T., Solomon, A., Sommerfeld, A., Spreen, G., Stephens, M., Stohl, A., Svensson, G., Uin, J., Viegas, J., Voigt, C., von der Gathen, P., Wehner, B., Welker, J. M., Wendisch, M., Werner, M., Xie, Z., and Yue, F.: Overview of the MOSAiC expedition—Atmosphere, Elementa: Sci. Anthrop., 10, https://doi.org/10.1525/elementa.2021.00060, 2022.

Shupe, M. D., Turner, D. D., Zwink, A., Theiman, M. M., Mlawer, M. J., and Shippert T. R.: Deriving Arctic cloud microphysics at Barrow: Algorithms, results, and radiative closure, J. Appl. Meteor. Clim., 54, 1675-1689, doi:10.1175/JAMC-D-15-0054.1, 2015.

Silber, I. and Shupe, M. D.: Insights on sources and formation mechanisms of liquid-bearing clouds over MOSAiC examined from a Lagrangian framework, Elementa: Sci. Anthrop., 10, 000071, https://doi.org/10.1525/elementa.2021.000071, 2022

Sivaraman, C., McFarlane, S., Chapman, E., Jensen, M., Toto, T., Liu, S., and Fischer, M.: Planetary Boundary Layer Height (PBL) Value Added Product (VAP): Radiosonde Retrievals, University of Maryland, United States, DOE/SC-ARM/TR-132, https://doi.org/10.2172/1808688, 2013.

Snyder, B. J. and Strawbridge, K. B.: Meteorological analysis of the Pacific 2001 air quality field study, Atmos. Environ., 38, 5733-5743, https://doi.org/10.1016/j.atmosenv.2004.02.068, 2004.

Solomon, A., Shupe, M. D., Persson, P. O. G., and Morrison, H.: Moisture and dynamical interactions maintaining decoupled Arctic mixed-phase stratocumulus in the presence of a humidity inversion, Atmos. Chem. Phys., 11, 10127-10148, https://doi.org/10.5194/acp-11-10127-2011, 2011.

Sørensen, J. H., Rasmussen, A., Ellermann, T., and Lyck, E.: Mesoscale influence on long-range transport — evidence from ETEX modelling and observations, Atmos. Environ., 32, 4207-4217,

907 https://doi.org/10.1016/S1352-2310(98)00183-6, 1998.

908 Sotiropoulou, G., Sedlar, J., Tjernström, M., Shupe, M. D., Brooks, I. M., and Persson, P. O. G.: The
909 thermodynamic structure of summer Arctic stratocumulus and the dynamic coupling to the surface,
910 Atmos. Chem. Phys., 14, 12573-12592, https://doi.org/10.5194/acp-14-12573-2014, 2014.

911 Steeneveld, G. J., van de Wiel, B. J. H., and Holtslag, A. A. M.: Comments on deriving the equilibrium
912 height of the stable boundary layer, Q. J. R. Meteorol. Soc., 133, 261-264, https://doi.org/10.1002/qj.26,
913 2007a.

914 Steeneveld, G. J., van de Wiel, B. J. H., and Holtslag, A. A. M.: Diagnostic Equations for the Stable
915 Boundary Layer Height: Evaluation and Dimensional Analysis, J. Appl. Meteor. Climatol., 46, 212-
916 225, https://doi.org/10.1175/JAM2454.1, 2007b.

917 Sterk, H. A. M., Steeneveld G. J., and Holtslag A. A. M.: The role of snow-surface coupling, radiation, and
918 turbulent mixing in modeling a stable boundary layer over Arctic sea ice, J. Geophys. Res.-Atmos., 118,
919 1199– 1217, https://doi.org/10.1002/jgrd.50158, 2013.

920 Tjernström, M., Balsley, B. B., Svensson, G., and Nappo, C. J.: The Effects of Critical Layers on Residual
921 Layer Turbulence, J. Atmos. Sci., 66, 468-480, https://doi.org/10.1175/2008jas2729.1, 2009.

922 Tjernström, M., Birch, C. E., Brooks, I. M., Shupe, M. D., Persson, P. O. G., Sedlar, J., Mauritsen, T., Leck,
923 C., Paatero, J., Szczodrak, M., and Wheeler, C. R.: Meteorological conditions in the central Arctic
924 summer during the Arctic Summer Cloud Ocean Study (ASCOS), Atmos. Chem. and Phys., 12, 6863-
925 6889, https://doi.org/10.5194/acp-12-6863-2012, 2012.

926 Tjernström, M. and Graversen, R. G.: The vertical structure of the lower Arctic troposphere analysed from
927 observations and the ERA-40 reanalysis, Q. J. R. Meteorol. Soc., 135, 431-443,
928 https://doi.org/10.1002/qj.380, 2009.

929 Uttal, T., Curry, J. A., McPhee, M. G., Perovich, D. K., Moritz, R. E., Maslanik, J. A., Guest, P. S., Stern,
930 H. L., Moore, J. A., Turenne, R., Heiberg, A., Serreze, M. C., Wylie, D. P., Persson, O. G., Paulson, C.
931 A., Halle, C., Morison, J. H., Wheeler, P. A., Makshtas, A., Welch, H., Shupe, M. D., Intrieri, J. M.,
932 Stamnes, K., Lindsey, R. W., Pinkel, R., Pegau, W. S., Stanton, T. P., and Grenfeld, T. C.: Surface Heat
933 Budget of the Arctic Ocean, Bull. Amer. Meteorol. Soc., 83, 255-276, https://doi.org/10.1175/1520-
934 0477(2002)083<0255:Shbota>2.3.Co;2, 2002.

935 Vihma, T.: Effects of Arctic Sea Ice Decline on Weather and Climate: A Review, Surv. Geophys., 35, 1175-
936 1214, https://doi.org/10.1007/s10712-014-9284-0, 2014.

937 Vihma, T., Kilpelainen, T., Manninen, M., Sjoblom, A., Jakobson, E., Palo, T., Jaagus, J., and Maturilli, M.:
938 Characteristics of Temperature and Humidity Inversions and Low-Level Jets over Svalbard Fjords in
939 Spring, Adv. Meteorol., 2011, 14, https://doi.org/10.1155/2011/486807, 2011.

940 Vogelezang, D. H. P. and Holtslag, A. A. M.: Evaluation and model impacts of alternative boundary-layer
941 height formulations, Boundary-Layer Meteorol., 81, 245-269, https://doi.org/10.1007/BF02430331,
942 1996.

943 Vullers, J., Achtert, P., Brooks, I. M., Tjernström, M., Prytherch, J., Burzik, A., and Neely, R.:
944 Meteorological and cloud conditions during the Arctic Ocean 2018 expedition, Atmos. Chem. and Phys.,
945 21, 289-314, https://doi.org/10.5194/acp-21-289-2021, 2021.

946 Wang, S., Wang, Q., Jordan, R. E., and Persson, P. O. G.: Interactions among longwave radiation of clouds,
947 turbulence, and snow surface temperature in the Arctic: A model sensitivity study, J. Geophys. Res.-
948 Atmos., 106, 15323-15333, https://doi.org/10.1029/2000JD900358, 2001.

949 Wetzel, C. and Bruemmer, B.: An Arctic inversion climatology based on the European Centre Reanalysis
950 ERA-40, Meteorologische Zeitschrift, 20, 589-600, https://doi.org/10.1127/0941-2948/2011/0295,
951 2011.

952 Zhang, J. A., Rogers, R. F., Nolan, D. S., and Marks, F. D.: On the Characteristic Height Scales of the
953 Hurricane Boundary Layer, Mon. Weather Rev., 139, 2523-2535, https://doi.org/10.1175/mwr-d-10-
954 05017.1, 2011.

955 Zhang, Y., Gao, Z., Li, D., Li, Y., Zhang, N., Zhao, X., and Chen, J.: On the computation of planetary

956   boundary-layer height using the bulk Richardson number method, Geosci. Model Dev., 7, 2599-2611,
957   https://doi.org/10.5194/gmd-7-2599-2014, 2014.

958   Zhang, Y. J., Sun, K., Gao Z. Q., Pan Z. T., Shook M. A., and Li D.,: Diurnal Climatology of Planetary
959   Boundary Layer Height Over the Contiguous United States Derived From AMDAR and Reanalysis
960   Data, J. Geophys. Res. Atmos., 125, https://doi.org/10.1029/2020JD032803, 2020.

961   Zilitinkevich, S. S.: On the determination of the height of the Ekman boundary layer, Boundary-Layer
962   Meteorol., 3, 141–145, https://doi.org/10.1007/BF02033914, 1972.

963   Zilitinkevich, S. S.: Third-order transport due to internal waves and non-local turbulence in the stably
964   stratified surface layer, Q. J. R. Meteorol. Soc., 128, 913–925,
965   https://doi.org/10.1256/0035900021643746, 2002.

966   Zilitinkevich, S. S.: The height of the atmospheric planetary boundary layer: State of the art and new
967   development, In H. J. S. Fernando, Z. Klaić, & J. McCulley (Eds.), National Security and Human Health
968   Implications of Climate Change (NATO Science for Peace and Security Series C: Environmental
969   Security) (pp. 147–161), Dordrecht: Springer. https://doi.org/10.1007/978-94-007-2430-3_13, 2012.

970   Zilitinkevich, S. S. and Baklanov, A.: Calculation Of The Height Of The Stable Boundary Layer In Practical
971   Applications, Boundary-Layer Meteorol., 105, 389–409, https://doi.org/10.1023/A:1020376832738,
972   2002.

973   Zilitinkevich, S. S., Elperin, T., Kleeorin, N., and Rogachevskii, I.: Energy- and flux-budget (EFB)
974   turbulence closure model for stably stratified flows. Part I: steady-state, homogeneous regimes.
975   Boundary-Layer Meteorol., 125, 167–191, https://doi.org/10.1007/s10546-007-9189-2, 2007.

976   Zilitinkevich, S. S. and Esau, I. N.: On Integral Measures Of The Neutral Barotropic Planetary Boundary
977   Layer, Boundary-Layer Meteorol., 104, 371–379. https://doi.org/10.1023/A:1016540808958, 2002.

978   Zilitinkevich, S. S. and Esau I. N.: The effect of baroclinicity on the depth of neutral and stable planetary
979   boundary layers, Q. J. R. Meteorol. Soc., 129, 3339–3356, https://doi.org/10.1256/qj.02.94, 2003
980
981